1

Layered Compounds in the In_2O_3–Ga_2O_3–ZnO System and Related Compounds in the Ternary System

1.1 Introduction

Indium–gallium–zinc oxide (IGZO) has gained traction as a novel semiconductor material in electronics. IGZO thin-film transistors are currently employed in the backplanes of mass-produced flat-panel displays, and their potential in various devices has been discussed in recent studies. The features and physical properties of IGZO differ from those of silicon, which is widely used in electronic devices. For instance, IGZO is a multi-component oxide with three cations. Furthermore, the distinctive layered structure of IGZO has led to the discovery of a new crystal morphology, *c*-axis-aligned crystalline IGZO (CAAC-IGZO), which will be detailed in the following chapters. The present chapter mainly describes the phase equilibrium diagrams of multi-component oxides and crystal structures of $InGaO_3(ZnO)_m$ ($m > 0$) with layered structures.

The properties of IGZO vary with the composition ratio of the metal elements. The bandgaps of In_2O_3, ZnO, and Ga_2O_3 (with different chemical compositions) are 2.6–2.9 [1, 2], 3.4 [3], and 4.8 eV [4], respectively. IGZO exhibits semiconductor properties in a relatively wide range of the phase equilibrium diagram. In the ZnO–$InGaZnO_4$ system, because ZnO and $InGaO_3(ZnO)$ ($m = 1$) show semiconductor properties, we speculate that a series of $InGaO_3(ZnO)_m$ will also behave as semiconductors. The $InGaO_3(ZnO)_m$ series has a layered structure in which O^{2-} is two-dimensional close-packed but may not be in contact with each other. This structure is closely related to the crystal morphology of CAAC-IGZO films, which will be described in the next chapter.

Physics and Technology of Crystalline Oxide Semiconductor CAAC-IGZO: Fundamentals, First Edition.
Edited by Noboru Kimizuka and Shunpei Yamazaki.

From the 1950s through the 1960s, the National Bureau of Standards [NBS, currently the National Institute of Standards and Technology (NIST)] in the United States comprehensively investigated the phase relationships of binary oxide systems such as R_2O_3–R'_2O_3, R_2O_3–A_2O_3, and R_2O_3–TiO_2 at temperatures up to 1800°C under atmospheric pressure. Here, R and R' denote lanthanides, Y, or Sc; A denotes Fe, Ga, Cr, or Al. Consequently, the NBS reported the thermochemical stability and crystal structures of the cationic elements in RAO_3 (perovskite), $R_3A_5O_{12}$ (garnet), magnetoplumbite, and $R_2Ti_2O_7$ (pyrochlore) [5–7]. Independently of the NBS research, Kimizuka and coworkers [8–17] added oxides of divalent cations, BO, to the binary system and investigated the resulting ternary system. This investigation, performed in the 1970s, is historically important as an extension of the NBS studies to a ternary system. In their systematic search for materials, Kimizuka and colleagues experimentally determined the phase equilibrium diagrams of the R_2O_3–A_2O_3–BO system at high temperatures and found a large number of $(RAO_3)_nBO$ and $RAO_3(BO)_m$. Here, R is a lanthanide, Y, In, or Sc; A is a trivalent cation and B is a divalent cation; m and n are natural numbers with no identified upper limits.

Subsequently, some $RAO_3(BO)_m$-type and $(RAO_3)_nBO$-type single crystals were grown, and their structures determined using single-crystal X-ray diffraction analysis. In addition, sintered powder bodies of these compounds were analyzed by powder X-ray diffraction and by electron beam diffraction. Consequently, the crystal structure of the homologous compounds $RAO_3(BO)_m$ was revealed: the R cation is located within the octahedral coordination of the O^{2-} anions, and the A and B cations are located within the trigonal-bipyramidal and tetrahedral coordination of the O^{2-} anions. All cations and anions in these oxides lie on the triangular lattice, and the O^{2-} anions stack perpendicular to the c-axis of the hexagonal crystal system [18–23]. The basic crystal structure was determined by analyzing $YbFe_2O_4$, an $RAO_3(BO)_m$ member with $m = 1$ [18]. The crystal structures of AB_2X_4-type compounds, classified by their coordination numbers, are listed in Table 1.1 [8, 24]. In the $YbFe_2O_4$-type crystal structure, R^{3+} occupies the sites of 6-fold oxygen octahedral coordination, and the A^{3+} and B^{2+} cations locate in the 5-fold oxygen trigonal-bipyramidal coordination. The $InGaO_3(ZnO)_m$ group $InGaO_3(ZnO)$ is isostructural with $YbFe_2O_4$. Before the discovery of $YbFe_2O_4$, no AB_2X_4-type compounds with 5- and 6-fold coordination were known. Compounds with layered structures related to $RAO_3(BO)_m$, including aluminum carbonitrides [25, 26] and sulfides (containing indium, gallium, and zinc), have also been reported [27].

Table 1.1 Classification of crystal structures with the general formula AB_2X_4, based on the coordination number (CN) of their cations. *Source*: Reprinted from [8], Copyright (1985), with permission from Elsevier

	CN of B				
CN of A	4	5	6	8	9 and/or 10
4	Phenacite		Olivine, spinel	K_2WO_4	β-K_2SO_4
6		$YbFe_2O_4$	Sr_2PbO_4, Ca_2IrO_4, etc.		K_2NiF_4
8			$CaFe_2O_4$, $CaTi_2O_4$		

As noted above, the R_2O_3–A_2O_3–BO system includes $RAO_3(BO)_m$ compounds with layered structures. In particular, layered $InGaO_3(ZnO)_m$ can be synthesized over a wide compositional range, and each $InGaO_3(ZnO)_m$ has substitutional solid solutions in the range $In_{1+x}Ga_{1-x}O_3(ZnO)_m (-1 < x \leq 1)$. Although structural uniformity is difficult to achieve in a multi-component system, such wide-ranging composition and solid solution suppresses the structural variation among the various chemical compositions. Therefore, the fundamental properties of layered crystals in the In_2O_3–Ga_2O_3–ZnO system, which are not expected to vary significantly, are suitable for the mass production of semiconductor devices. Kimizuka's elucidation of the phase equilibrium in In_2O_3–Ga_2O_3–ZnO has contributed significantly to the subsequent technology and mass production of CAAC-IGZO devices.

As a prelude to the succeeding chapters, this chapter introduces the crystal structures and phase equilibrium diagrams at high temperatures in the R_2O_3–A_2O_3–BO system, including the layered oxides mentioned above. Section 1.2 describes the phase equilibrium diagrams of ternary systems, including $InGaO_3(ZnO)_m$, and shows that their characteristics are not limited to the In_2O_3–Ga_2O_3–ZnO system. Section 1.3 presents the crystal structure of $InGaO_3(ZnO)_m$ and its layer-stacking sequences, obtained in a crystal structure analysis of powdered and single-crystal specimens. Section 1.4 presents transmission electron microscopy (TEM) images of $InGaO_3(ZnO)_m$ (where m is non-integer) with a long-period disordered stacking sequence along an axis perpendicular to the layer. The methods used to acquire the scanning TEM (STEM) images [annular bright field (ABF) and high-angle annular dark field (HAADF)] are outlined in Appendix 1.A.

1.2 Syntheses and Phase Equilibrium Diagrams

Here we describe what led to the discovery of $InGaZnO_4$. The first important study was on a phase equilibrium diagram of the Y_2O_3–Fe_2O_3–FeO system at high temperatures [19, 28]. This system includes YFe_2O_4, a mixed-valence compound containing Fe^{2+} and Fe^{3+} which is isostructural with $InGaZnO_4$. Subsequently, the phase equilibrium diagram of the R_2O_3–Fe_2O_3–FeO system (R = Ho, Er, Tm, Yb, and Lu) was determined [29–32], and a new phase $(RFeO_3)_nFeO$ $(n > 0)$ with members $(RFeO_3)$ FeO, $(RFeO_3)_2$ FeO, … was found. $RFeO_3(FeO)$ and $(RFeO_3)_2(FeO)$are isostructural with $InGaO_3(ZnO)$ and $(InGaO_3)_2ZnO$, respectively.

When determining the phase relationships of the above-mentioned systems comprising FeO, the oxygen partial pressure $P(O_2)$ must be controlled. The phase equilibrium diagrams of these systems were determined in situ using thermogravimetric analysis, controlling the $P(O_2)$ in the gas phase. Among these systems, Y_2O_3–Fe_2O_3–FeO and Yb_2O_3–Fe_2O_3–FeO were particularly selected as case studies in Subsection 1.2.1.

The phase equilibrium diagram of the ternary system R_2O_3–A_2O_3–BO (R= a lanthanide element, In, or Sc; A = In, Fe, Ga, or Al; B = Mg, Mn, Co, Cu, or Zn) was determined from solid-phase reactions of R_2O_3, A_2O_3, and BO powders [8, 11]. These compounds were synthesized with the classical quenching method, in which the starting materials were sealed in platinum tubes and the mixtures rapidly cooled in water after heating for a predetermined time. The diagrams were constructed from the crystal structures of the synthesized powders, as identified by powder X-ray diffraction and electron beam diffraction methods. For example, the following compounds were discovered: $In_2O_3(ZnO)_m$ [23, 33–37], $InAlO_3(ZnO)_m$ [16], $InFeO_3(ZnO)_m$ [10, 14, 21], $(InFeO_3)_n(CuO)_m$ [9], $(InGaO_3)_n(CuO)_m$ [9], $InFeO_3(MnO)_m$ [38], and

$InGaO_3(MnO)_m$ [12], all of which are isostructural with $InGaO_3(ZnO)_m$ [8, 11, 15, 23, 39]. Among these, the $In_2O_3-Ga_2O_3-BO$ system (B = Zn, Mg, Cu, and Co) is discussed in Subsection 1.2.2.

As mentioned above, a series of phases is generally expressed by a composition formula with a certain variable (e.g., a natural number n). These phases are called "homologous[1] phases." For example, the series of vanadium oxide compounds VO_2, V_2O_3, V_3O_5, … is defined by the general formula V_nO_{2n-1}. Such phases are called Magnéli phases; meanwhile, phases with the general formula V_nO_{2n+1} are called Wadsley phases. Although Magnéli and Wadsley phases are given by different formulae, in the context of this book, these phases belong to the homologous phase. As described in Section 1.1, the compounds $InGaO_3(ZnO)$, $InGaO_3(ZnO)_2$, $InGaO_3(ZnO)_3$, … are generally referred to as homologous-phase $InGaO_3(ZnO)_m$; compounds belonging to homologous phases are termed "homologous compounds," and homologous compounds with the composition formula $InGaO_3(ZnO)$ are termed "homologous $InGaO_3(ZnO)$."

1.2.1 Phase Equilibrium Diagrams in the System $R_2O_3-Fe_2O_3-FeO$ (R = Y and Yb)

(RFeO$_3$) FeO (R = Y and Yb) and (RFeO$_3$)$_2$ FeO are isostructural with ($InGaO_3$)ZnO and ($InGaO_3$)$_2$ZnO, respectively. This subsection describes the Y_2O_3–Fe_2O_3–Fe and Yb_2O_3–Fe_2O_3–Fe systems, from which the homologous (RFeO$_3$)$_n$(BO) were synthesized. The phase equilibrium diagrams of these systems were determined in situ by thermogravimetric analysis under controlled oxygen partial pressure $P(O_2)$. Thermogravimetric analysis directly measures the weight change of a sample heated at a constant rate using a thermobalance. The total pressure is 1 atm, and the oxygen partial pressure is controlled by the mixing ratio of the CO_2 and H_2 gas. In analyzing the above systems, the temperature was set to 1200°C, and the oxygen partial pressure (measured using a stabilized zirconia electrolyte cell) was increased from 1.0 to 1.58×10^{-16} atm.

1.2.1.1 Y_2O_3–Fe_2O_3–FeO System at 1200°C

As mentioned above, the phase equilibrium diagram of the Y_2O_3–Fe_2O_3–Fe system was determined at 1200°C [19, 28]; we describe the subsystem Y_2O_3–Fe_2O_3–FeO. In this subsystem, Y_2O_3, Fe_2O_3 (hematite) and FeO (wüstite) have bixbyite, corundum, and rock salt structures, respectively. The binary Y_2O_3–Fe_2O_3 system includes $YFeO_3$ (distorted perovskite) and $Y_3Fe_5O_{12}$ (yttrium–iron garnet). The binary Fe_2O_3–FeO system has Fe_3O_4 (magnetite) with Fe^{2+} and Fe^{3+}. YFe_2O_4, a new phase composed of Y_2O_3–Fe_2O_3–FeO, lies between $YFeO_3$

[1] The term "homologous" has various meanings in different fields. For example, in biology, "homologous" means "corresponding in structure and in origin," as for example the wing of a bird and the foreleg of a horse [A: *Random House Dictionary*]. In organic chemistry, "homologous" refers to a series of organic compounds "having similar characteristics and structure but differing by a number of CH_2 groups" [B: *Collins English Dictionary*]. In crystal chemistry, the term is used for a series of compounds expressed by a general formula. For example, IGZO has a series of compounds group, e.g., $In_2Ga_2ZnO_7$, $InGaZn_2O_5$, $InGaZn_3O_6$, and so on. These compounds are called a "homologous" series.

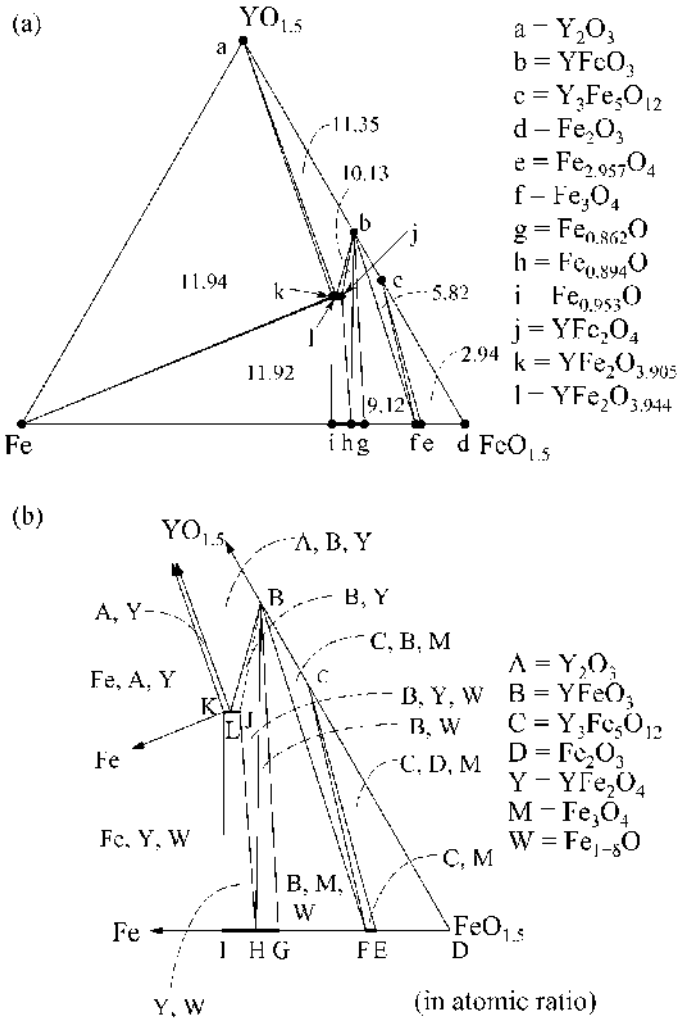

Figure 1.1 (a) Phase equilibrium diagram of the Y_2O_3–Fe_2O_3–Fe system at 1200°C and (b) detailed phase equilibrium diagram near $FeO_{1.5}$. ●, Single phase. In (a), the numbers signify the values of the $-\log P(O_2)$ fields equilibrated with the three solid phases. Small letters (a to l) in the diagram represent a chemical composition of a single phase as in the right of this figure. In (b), capital letters (A to M, W, and Y) in the diagram represent a phase of a chemical composition: letters A to L correspond to the small letters a to l in (a); letters M, W, and Y are as shown in the right of this figure. M is magnetite solid solution, W is partial solid solution of wüstite, and Y is solid solution or partial solid solution of YFe_2O_4. *Source*: Adapted from [28]

and FeO (shown in Figure 1.1) [28]. The YFe_2O_4 phase is isostructural with $InGaO_3(ZnO)$, as described later, and constitutes a mixed-valence compound with a layered structure of Fe^{2+} and Fe^{3+}. YFe_2O_4 was grown under controlled oxygen partial pressure by the floating zone method, and its crystal structure was determined by X-ray diffraction [19].

This YFe_2O_4 phase is stable at oxygen partial pressures $P(O_2)$ from 7.41×10^{-11} to 1.14×10^{-12} atm, and its chemical composition varies from $YFe_2O_{3.905}$ to $YFe_2O_{4.000}$. Above this $P(O_2)$ range, it decomposes into Y_2O_3 and metallic iron (γ-iron); below this range, it dissociates into $YFeO_3$ and wüstite (FeO). This dissociation is also observed at temperatures between 900 and 1100°C at a pressure of 4.9 GPa. A melt phase emerges at 1400°C. Under atmospheric pressure at 800°C, the YFe_2O_4 phase dissociates into an E phase (with a chemical composition of $Fe_{2.957}O_4$) and wüstite (FeO).

1.2.1.2 Yb_2O_3–Fe_2O_3–FeO System at 1200°C

Subsequent to the Y_2O_3–Fe_2O_3–Fe system, the next phase equilibrium diagram was constructed for the Yb_2O_3–Fe_2O_3–Fe system at 1200°C [29]; we describe the subsystem Yb_2O_3–Fe_2O_3–FeO. Homologous $(YbFeO_3)_nFeO$ (n = 1, 2, 3, and 4) were found as a new phase of this ternary system. Yb_2O_3 is a sesquioxide isostructural with the mineral bixbyite, similar to the above-mentioned Y_2O_3. However, the ionic radius of Yb^{3+} is smaller than that of Y^{3+} [40]. As with the Y_2O_3–Fe_2O_3–Fe system, the thermal equilibrium state of this system was analyzed at 1200°C under controlled partial oxygen pressure. In the $YbFeO_3$–FeO system, $YbFe_2O_4$ and $Yb_2Fe_3O_7$ are stable at oxygen partial pressures $P(O_2)$ ranging from 1.66×10^{-12} to 5.01×10^{-9} and 2.00×10^{-10} to 5.01×10^{-9} atm, respectively. Single crystals of $(YbFeO_3)$FeO and $(YbFeO_3)_2$FeO were grown, and their crystal structures were revealed [41]. Like the compounds in the Y_2O_3–Fe_2O_3–FeO system, the $YbFe_2O_4$ [18, 29] and $Yb_2Fe_3O_7$ [29, 42] in the Yb_2O_3–Fe_2O_3–FeO system are mixed-valence phases of Fe^{2+} and Fe^{3+}. These phases are isostructural with $InGaO_3(ZnO)$ and $(InGaO_3)_2ZnO$, respectively, as mentioned later. Figure 1.2 shows the phase equilibrium diagram of the Yb_2O_3–Fe_2O_3–FeO system at 1200°C. Note that $Yb_3Fe_4O_{10}$ and $Yb_4Fe_5O_{13}$ are generated as the heating temperature increases [43, 44].

1.2.2 Phase Equilibrium Diagram for the System In_2O_3–A_2O_3–BO (A = Ga and Fe; B = Zn, Mg, Cu, and Co)

In the phase equilibrium diagrams of the system R_2O_3–Fe_2O_3–FeO (R = Y and Yb), new phases were found; namely, YFe_2O_4 and $(YbFeO_3)_n$(FeO) (n = 1, 2, 3, and 4). Subsequently, the lanthanide element was replaced with an element of smaller ionic radius (indium), and the phase equilibrium diagram of the resulting system In_2O_3–A_2O_3–BO (where A is a trivalent cation and B is a divalent cation) was comprehensively investigated.

This subsection focuses on the relationship between the component BO (B = Zn, Mg, Cu, and Co) and the phase equilibrium diagram of the system In_2O_3–Ga_2O_3–BO. In these systems, each oxide has the following features: indium has a smaller ionic radius than a lanthanide; In_2O_3, like Y_2O_3 and Yb_2O_3, is isostructural with the mineral bixbyite. The indium cation in the oxide is trivalent with 4-, 5-, 6-, and 8-fold coordination [40]. In contrast, 4- and 5-fold coordination is unknown in rare-earth elements. The gallium oxide is isostructural with β-Ga_2O_3. The trivalent gallium cation has coordination numbers of four, five, and six. Empirically, trivalent gallium cations are known to favor four-coordinate cations more than trivalent iron cations. The divalent cations (B^{2+}) of Zn^{2+}, Co^{2+}, and Cu^{2+} are more inclined to be 4-fold coordinated

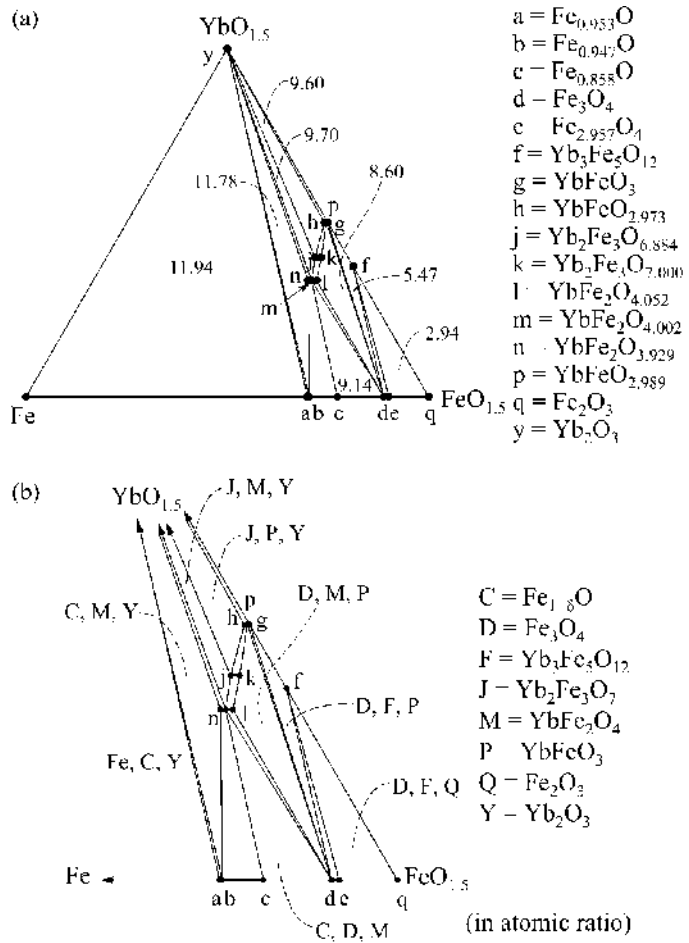

Figure 1.2 (a) Phase diagram of the system Yb_2O_3–Fe_2O_3–Fe at 1200°C and (b) detailed phase equilibrium diagram near $FeO_{1.5}$. ●, Experimental results. In (a), the numbers signify the values of the $-\log P(O_2)$ fields equilibrated with the three solid phases. Small letters (a to n, p, q, and y) in the diagram represent a chemical composition as in the right of this figure. In (b), capital letters in the diagram represent a phase corresponding to a chemical composition as in the right of this figure. These letters correspond to the small letters in (a). Solid solution of $YbFe_2O_4$ and $Yb_2Fe_3O_7$ exists in the range from l to n, and from j to k. $YbFe_2O_4$ and $Yb_2Fe_3O_7$ belong to homologous $(YbFeO_3)_n(FeO)$. *Source*: Adapted from [29]

than Fe^{2+}. The 4-fold coordination geometry of Co^{2+} and Cu^{2+} differs from that of Zn^{2+}, resulting in the difference in their crystallographic behavior.

In Subsections 1.2.2.1–1.2.2.4 we explain the phase equilibrium diagrams of two In_2O_3–Ga_2O_3–BO systems. In the first instance, B = Zn; in the second instance, B = Mg, Cu, and Co.

1.2.2.1 In_2O_3–Ga_2O_3–ZnO System at 1350°C

Under atmospheric pressure, the In_2O_3, Ga_2O_3, and ZnO in the In_2O_3–Ga_2O_3–ZnO system exhibit a bixbyite-type structure, a β-Ga_2O_3-type structure, and a wurtzite-type structure, respectively. At high temperature, Ga_2O_3 is a mineral corundum, as is Fe_2O_3. The In_2O_3–ZnO system contains hexagonal $In_2O_3(ZnO)_m$, whereas the Ga_2O_3–ZnO system contains orthorhombic $Ga_2O_3(ZnO)_m$. Likewise, the In_2O_3–Ga_2O_3–ZnO system contains $(InGaO_3)_2ZnO$ and $InGaO_3(ZnO)_m$. Figure 1.3 shows the phase diagram of the In_2O_3–Ga_2O_3–ZnO system. The regions (1)–(5) in this figure are explained below.

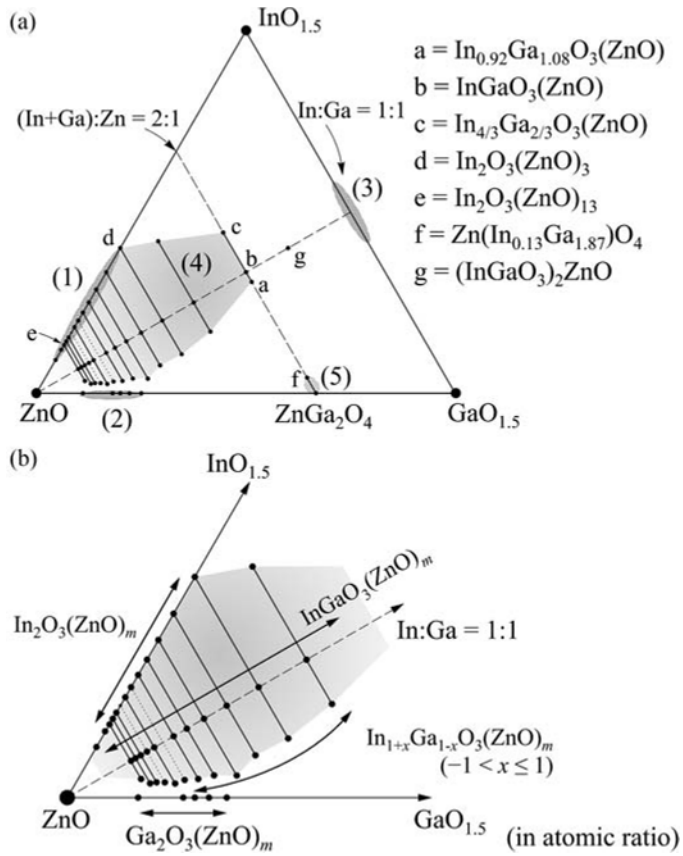

Figure 1.3 (a) Phase equilibrium diagram in the In_2O_3–Ga_2O_3–ZnO system at 1350°C and (b) detailed phase equilibrium diagram near ZnO. Filled circles (●) and solid lines connecting two filled circles are a single phase. (a) Small letters (a to g) in the diagram represent a chemical composition as in the right of this figure. Regarding homologous compounds, the solid lines connecting $In_2O_3(ZnO)_m - InGaO_3(ZnO)_m - In_{1+x}Ga_{1-x}O_3(ZnO)_m$ with the same m denote the solid-solution range. $InGaO_3(ZnO)_m$ and $InGaO_3(ZnO)_m$ have a hexagonal lattice, and $Ga_2O_3(ZnO)_m$ has an orthorhombic lattice. *Source*: Adapted from [15]

Region (1)

The In_2O_3–ZnO system contains $In_2O_3(ZnO)_m$ ($m \geq 3$). Kasper [33] reported on $In_2O_3(ZnO)_m$ ($m = 2, 3, 4, 5, 7$), Cannard and Tilley [34] reported on $In_2O_3(ZnO)_m$ ($m = 4, 5, 6, 7, 9, 11$), and Dupont *et al.* [35] reported on $In_2O_3(ZnO)_m$ ($m = 90$). $In_2O_3(ZnO)_m$ ($m = 5, 7$) does not decompose at temperatures above 1100°C; the other $In_2O_3(ZnO)_m$ single phases are stable at higher temperatures. For example, $In_2O_3(ZnO)_3$ is stable at 1265°C or higher, but decomposes into In_2O_3 and $In_2O_3(ZnO)_5$ at 1190°C, and into In_2O_3 and $In_2O_3(ZnO)_4$ at 1200°C [23].

Region (2)

The Ga_2O_3–ZnO system contains $ZnGa_2O_4$ (spinel type [45]) and $Ga_2O_3(ZnO)_m$ [46–49]. The crystal lattice of $Ga_2O_3(ZnO)_m$ is orthorhombic and differs from the hexagonal crystal lattice of $InGaO_3(ZnO)_m$. In the $Ga_2O_3(ZnO)_m$ crystal structure, all cations have 4-fold or 5-fold oxygen coordination; 6-fold coordination is not observed.

Region (3)

Under atmospheric pressure, the In_2O_3–Ga_2O_3 system has solid-solution phases of β-Ga_2O_3 and bixbyite In_2O_3; these phases co-exist at an In:Ga atomic ratio of 1:1. Hexagonal $InGaO_3$ is unstable under atmospheric pressure, but $InGaO_3$ isostructural with $YAlO_3$ forms under pressures higher than 0.3–1.5 GPa at 1100°C [50].

Region (4)

In the $InGaO_3$–ZnO system, $(InGaO_3)_2(ZnO)$ and $InGaO_3(ZnO)_m$ ($m \geq 1$) are present. $InGaO_3(ZnO)$ is isostructural with $YbFeO_3(FeO)$. An X-ray powder diffraction pattern confirms that $(InGaO_3)_2(ZnO)$ is isostructural with $(YbFeO_3)_2FeO$, although single crystals of this compound have yet to be synthesized. Layered structures in the $InGaO_3$–ZnO system can be approximately derived by stacking CdI_2-type and wurtzite-type structures, or by stacking $YAlO_3$-type and wurtzite-type structures. These crystal structures will be explained in Section 1.3. The In_2O_3–$ZnGa_2O_4$–ZnO system forms a solid solution of each $InGaO_3(ZnO)_m$ phase, and its solid solution ranges as $In_{1+x}Ga_{1-x}O_3(ZnO)_m$ ($m \geq 1$, $-1 < x \leq 1$, where x depends on m). When $m \geq 3$, the indium solid-solution limit of $In_{1+x}Ga_{1-x}O_3(ZnO)_m$ corresponds to $In_2O_3(ZnO)_m$ in the binary In_2O_3–ZnO system. In other words, solid solutions exist in the range $In_2O_3(ZnO)_m$ to $InGaO_3(ZnO)_m$ (Figure 1.3). Ga-rich compositions in the range $InGaO_3(ZnO)_m$ to $In_{1+x}Ga_{1-x}O_3(ZnO)_m$ ($m \geq 1$, $-1 < x < 0$) also form solid solutions [15, 39]. Layered Ga-rich structures form solid solutions over a narrow range; thus, no $Ga_2O_3(ZnO)_m$ is isostructural with $InGaO_3(ZnO)_m$. For example, in $(In + Ga) : Zn = 2 : 1$ (atomic ratio), $InGaO_3(ZnO)$ forms a solid solution in the range $In_{1.33}Ga_{0.67}O_3(ZnO)$ to $In_{0.92}Ga_{1.08}O_3(ZnO)$. Note that the system In_2O_3–A_2O_3–ZnO (A = Fe, Al) [14, 16] also contains $InAO_3(ZnO)_m$, which is isostructural with $InGaO_3(ZnO)_m$.

Region (5)

In $(In + Ga) : Zn = 2 : 1$ (atomic ratio), spinel-type $ZnGa_2O_4$ forms at the Ga-rich limit. The upper limit of the indium solid-solution range of $ZnGa_2O_4$ is approximately 3 mol% [15].

1.2.2.2 In_2O_3–Ga_2O_3–MgO System at 1300°C

In addition to the In_2O_3–Ga_2O_3–ZnO system, the In_2O_3–Ga_2O_3–BO system is likely to contain compounds isostructural with $(YbFeO_3)_nFeO$ and $InGaO_3(ZnO)_m$ and their solid solutions. The presence of such groups of compounds and their solid solutions depends on the combination of trivalent cations (In^{3+}, Ga^{3+}) and divalent cations. Here we describe the In_2O_3–Ga_2O_3–MgO system, which has a group of layered-structure compounds isostructural with the In_2O_3–Ga_2O_3–ZnO system, and whose spinel-type $MgGa_2O_4$ ($MgIn_2O_4$) has a wide range of substitutional solid solutions involving indium (gallium) cations.

The phase equilibrium diagram of the In_2O_3–Ga_2O_3–MgO system at 1300°C [13] allows layered-structure $InGaO_3(MgO)_m$ ($m = 1, 2$) and spinel-type $MgGa_2O_4$ (shown in Figure 1.4) [51, 52]. $InGaO_3(MgO)$ and $InGaO_3(MgO)_2$ are isostructural with $InGaO_3(ZnO)$ and $InGaO_3(ZnO)_2$, respectively. $InGaO_3(MgO)$ forms a solid solution in the composition range $InGaO_3(MgO)$ to $In_{1+x}Ga_{1-x}O_3(MgO)(x = 0.2)$ (solid line R–S in Figure 1.4). Like $InGaO_3(ZnO)$, $InGaO_3(MgO)$ retains its layered structure at various composition ratios of trivalent cations (In^{3+}, Ga^{3+}).

Unlike the In_2O_3–Ga_2O_3–ZnO system, the $MgIn_2O_4$–$MgGa_2O_4$ system has a wide range of spinel-type solid solutions. In the range $Mg(In_{2-x}Ga_x)O_4$ ($0 \le x \le 0.32$), Ga_2O_3 and $MgIn_2O_4$ are dissolved (solid line P–Q in Figure 1.4), whereas in the range $Mg(In_xGa_{2-x})O_4$ ($0 \le x \le 0.40$), In_2O_3 and $MgGa_2O_4$ mix (solid line U–V in Figure 1.4). In solid solutions of $MgIn_2O_4$ in which Ga substitutes for In, and of $MgGa_2O_4$ in which In substitutes for Ga, $Mg(In_{2-x}Ga_x)O_4$ and $Mg(In_xGa_{2-x})O_4$ have an inverse spinel-type structure.

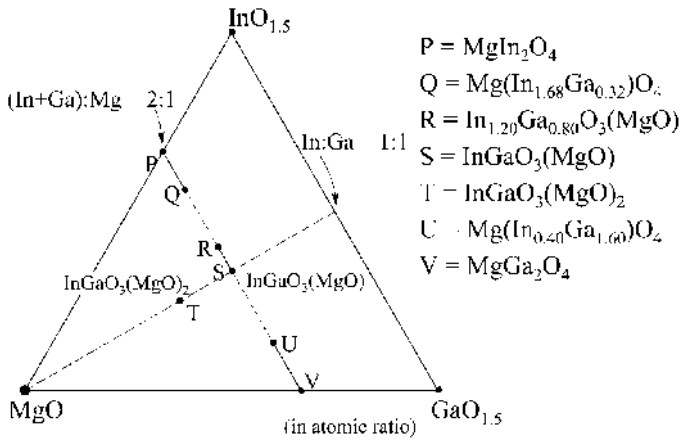

Figure 1.4 Phase equilibrium diagram in the In_2O_3–Ga_2O_3–MgO system at 1300°C. Filled circles (●) and solid lines connecting two filled circles are a single phase. Capital letters (P to V) in the diagram represent a chemical composition as in the right of this figure. At the triangle vertexes corresponding to $InO_{1.5}$, $GaO_{1.5}$, and MgO, the single phases In_2O_3, Ga_2O_3, and MgO exist, respectively. The line between P and V denotes $(In + Ga) : Mg = 2 : 1$. The dashed line extending from MgO denotes $In : Ga = 1 : 1$. The solid lines P–Q and U–V indicate a solid-solution range of the spinel-type structure, and the solid line R–S indicates a solid-solution range of the $YbFe_2O_4$-type structure. *Source*: Adapted from [13]

As mentioned above, the multi-component oxides of the In_2O_3–Ga_2O_3–MgO system have a narrow composition range for layered structures and a wide range for spinel-type structures. When $(In + Ga) : Mg = 2 : 1$, spinel-type structures form in the In-rich and Ga-rich limits, whereas layered structures form when In and Ga have approximately the same chemical composition.

1.2.2.3 In_2O_3–Ga_2O_3–CuO System at 1000°C

The In_2O_3–Ga_2O_3–CuO system substitutes Cu^{2+} for Zn^{2+} in the In_2O_3–Ga_2O_3–ZnO system. At 1000°C, this system includes bixbyite-type In_2O_3, β-Ga_2O_3-type Ga_2O_3, tenorite-type CuO, spinel-type $CuGa_2O_4$, and $Ho_2Cu_2O_5$-type $In_2Cu_2O_5$ [53]. The $InGaO_3$–CuO system includes $(InGaO_3)CuO$ and $(InGaO_3)_2CuO$, which are isostructural with $(YbFeO_3)FeO$ and $(YbFeO_3)_2FeO$, respectively. The homologous phases in the In_2O_3–Ga_2O_3–CuO system are shown in Figure 1.5, and their lattice constants are shown in Table 1.2. A phase isostructural

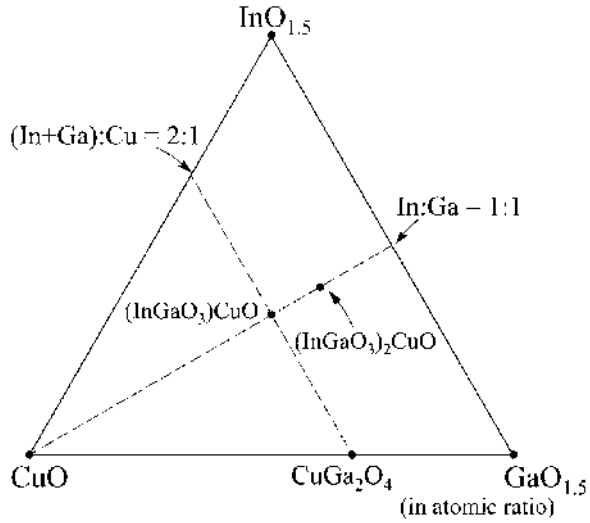

Figure 1.5 Phase equilibrium diagram in the In_2O_3–Ga_2O_3–CuO system at 1000°C. ● Indicates that $InGaO_3(CuO)$ and $(InGaO_3)_2CuO$ are isostructural with $YbFeO_3(FeO)$ and $(YbFeO_3)_2FeO$, respectively. *Source*: Adapted from [9]

Table 1.2 Lattice constants of homologous compounds in $(InGaO_3)_nCuO$ and $(InGaO_3)_nZnO$, both shown in a hexagonal system. *Source*: Adapted from [9, 15]

	$(InGaO_3)CuO$ [9]	$(InGaO_3)ZnO$ [15]
a [nm]	0.3350	0.3296
c [nm]	2.482	2.602
	$(InGaO_3)_2CuO$	$(InGaO_3)_2ZnO$
a [nm]	0.3332	0.3306
c [nm]	2.870	2.946

with $InGaO_3(ZnO)_m$ ($m \geq 2$) and its solid solution are not found, because the coordination geometry differs between Cu^{2+} and Zn^{2+}. CuO and ZnO have 4-fold oxygen coordination but exhibit different coordination geometry; square planar and tetrahedral, respectively. Therefore, the compounds in the In_2O_3–Ga_2O_3–CuO system are not isostructural with $InGaO_3(ZnO)_m$ ($m \geq 2$).

1.2.2.4 In_2O_3–Ga_2O_3–CoO System at 1300°C

At 1300°C, the In_2O_3–Ga_2O_3–CoO system includes bixbyite-type In_2O_3, β-Ga_2O_3-type Ga_2O_3, NaCl-type CoO, and spinel-type $CoGa_2O_4$. $InGaO_3(CoO)$ isostructural with $YbFe_2O_4$ also exists; however, there have been no reports on $(InGaO_3)_nCoO$ ($n \geq 2$), $InGaO_3(CoO)_m$ ($m \geq 2$), and a solid solution of $InGaO_3(CoO)$. The solid solution $Co(In_xGa_{2-x})O_4$ of indium-substituted $CoGa_2O_4$ is in the range $0.0 \leq x \leq 0.4$. The phase diagram of the In_2O_3–Ga_2O_3–CoO system (Figure 1.6) resembles that of In_2O_3–Ga_2O_3–MgO rather than In_2O_3–Ga_2O_3–ZnO, although the In_2O_3–CoO system contains no spinel-type $CoIn_2O_4$.

1.2.3 Phase Equilibrium Diagram of the System In_2O_3–A_2O_3–ZnO (A = Fe and Al)

The previous subsection described the phase diagram of the In_2O_3–Ga_2O_3–BO system (B = Zn, Mg, Cu, and Co), whose element combination determines the chemical composition ranges of

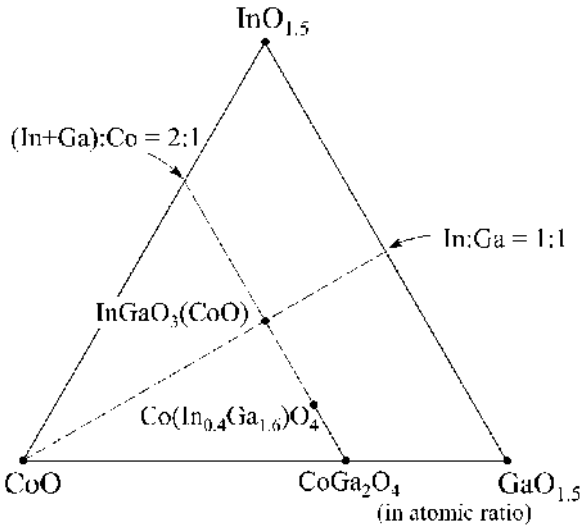

Figure 1.6 Phase equilibrium diagram in the In_2O_3–Ga_2O_3–CoO system at 1300°C. Plotted are $YbFe_2O_4$-type $InGaO_3(CoO)$ and spinel-type $CoGa_2O_4$. Indium solid solution of $CoGa_2O_4$ exists up to $In_{0.4}Ga_{1.6}O_3(CoO)$. The solid line shows the indium solid-solution range of $CoGa_2O_4$. *Source*: Adapted from [9]

the homologous compounds and the solid solutions. In fact, some $InGaBO_4$-type compounds are reported to contain compounds that take both layered and spinel-type structures; the In_2O_3–Ga_2O_3–MnO system contains spinel-type and $YbFe_2O_4$-type $InGaMnO_4$ [8].

Within the system In_2O_3–Ga_2O_3–BO (B = Zn, Mg, Cu, and Co), the In_2O_3–Ga_2O_3–ZnO system has the largest number of homologous phases, and $InGaO_3(ZnO)_m$ has a wide solid-solution range. This indicates that ZnO is currently the best combination for forming layered structures over a wide chemical-composition range in ternary oxide systems including In_2O_3 and Ga_2O_3.

The $In_2O_3 - A_2O_3 - ZnO$ (A = Ga, Fe, and Al) system forms layered structures over an extensive range of chemical compositions [14, 16]. The phase equilibrium diagram of the In_2O_3–Ga_2O_3–ZnO system was presented in Subsection 1.2.2.1; we now present the phase diagram of In_2O_3–A_2O_3–ZnO (A = Fe and Al).

1.2.3.1 In_2O_3–Fe_2O_3–ZnO System at 1350°C

Under atmospheric pressure, In_2O_3, Fe_2O_3, and ZnO in the In_2O_3–Fe_2O_3–ZnO system exhibit bixbyite-type, corundum-type, and wurtzite-type structures, respectively. The In_2O_3–ZnO system includes homologous compounds of the form $In_2O_3(ZnO)_m$. Likewise, the In_2O_3–Fe_2O_3–ZnO system includes homologous compounds of the form $InFeO_3(ZnO)_m$. The phase diagram of the In_2O_3–Fe_2O_3–ZnO system is shown in Figure 1.7. Regions (1)–(4) in that figure are explained below.

Region (1)

The In_2O_3–ZnO system contains $In_2O_3(ZnO)_m$ ($m \geq 3$) (see Subsection 1.2.2.1).

Region (2)

In addition to spinel-type $ZnFe_2O_4$, the Fe_2O_3–ZnO system includes $Fe_2O_3(ZnO)_m$ ($m = 12, 13$) [14], which is not isostructural with $InFeO_3(ZnO)_m$. $Fe_2O_3(ZnO)_m$ with smaller m exist at 1550°C [21].

Region (3)

In the $InFeO_3$–ZnO system, $InFeO_3(ZnO)_m$ ($m \geq 1$) is present. As with $InGaO_3(ZnO)$, $InFeO_3(ZnO)$ is isostructural with $YbFeO_3(FeO)$. In the In_2O_3–$ZnFe_2O_4$–ZnO system, each phase of $InFeO_3(ZnO)_m$ has a solid solution in the range $In_{1+x}Fe_{1-x}O_3(ZnO)_m$ ($m \geq 1$, $-1 < x \leq 1$, x depends on m). When $m \geq 3$, the limit of indium solid solution is $In_2O_3(ZnO)_m$. Solid solutions also form in Fe-rich compositions [14] over ranges that depend on m. Note that $In_{1+x}Fe_{1-x}O_3(ZnO)_m$ solid solutions exclude $Fe_2O_3(ZnO)_m$ in region (2), because this compound is not isostructural with $InFeO_3(ZnO)_m$.

Region (4)

The chemical composition $(In + Fe) : Zn = 2 : 1$ (atomic ratio) admits spinel-type $ZnFe_2O_4$. The indium solid solution of this compound ranges from $ZnFe_2O_4$ to $In_xFe_{2-x}O_3(ZnO)_4$.

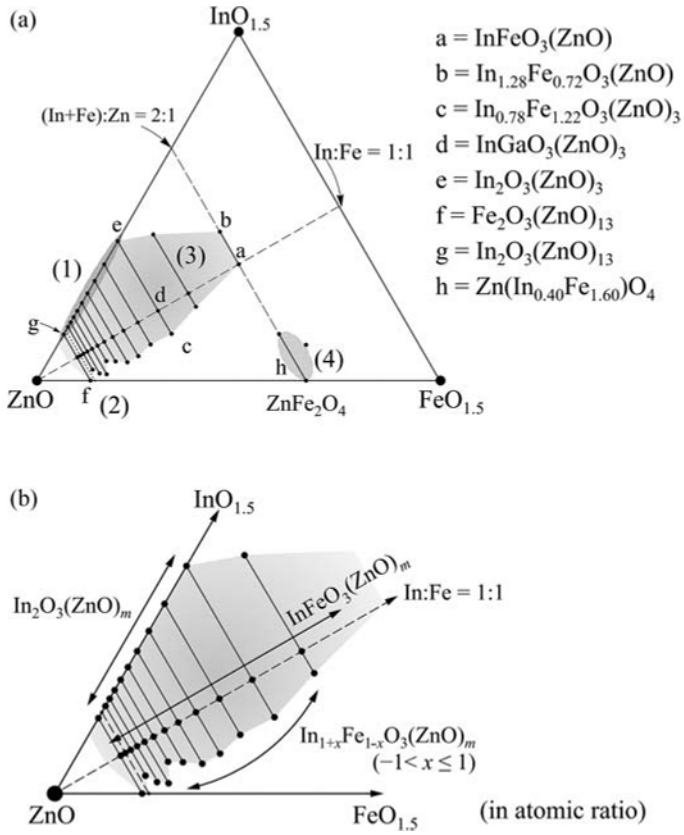

Figure 1.7 (a) Phase equilibrium diagram of the In_2O_3–Fe_2O_3–ZnO system at 1350°C and (b) detailed phase equilibrium near ZnO. Solid lines indicate the solid-solution ranges of single-phase $InFeO_3(ZnO)_m$, and the dashed line shows the undetermined range. Filled circles (●) and solid lines connecting two filled circles are a single phase. In (a), small letters (a to h) in the diagram represent a chemical composition as in the right of this figure. *Source*: Adapted from [14]

1.2.3.2 In_2O_3–Al_2O_3–ZnO System at 1350°C

Under atmospheric pressure, the In_2O_3, Al_2O_3, and ZnO in the In_2O_3–Al_2O_3–ZnO system exhibit bixbyite-type, corundum-type, and ZnO wurtzite-type structures, respectively. The In_2O_3–ZnO and In_2O_3–Al_2O_3–ZnO systems include homologous compounds with compositions $In_2O_3(ZnO)_m$ and $InAlO_3(ZnO)_m$, respectively. The Al_2O_3–ZnO system has spinel-type $ZnAl_2O_4$, for which no homologous compounds exist in this ternary Al_2O_3–ZnO system. Here we describe the In_2O_3–Al_2O_3–ZnO system from regions (1) to (3) in Figure 1.8.

Region (1)

As described in Subsection 1.2.2.1, the In_2O_3–ZnO system includes $In_2O_3(ZnO)_m$ ($m \geq 3$).

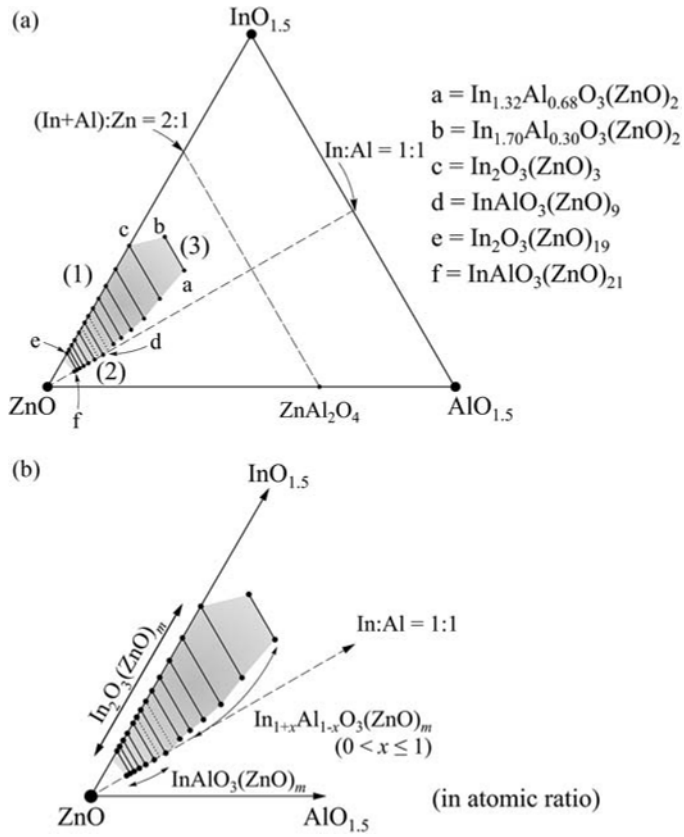

Figure 1.8 (a) Phase equilibrium diagram in the In_2O_3–Al_2O_3–ZnO system at 1350°C and (b) detailed phase equilibrium near ZnO. Solid lines indicate the solid-solution ranges of single-phase $InAlO_3(ZnO)_m$, and the dashed lines are the undetermined solid-solution ranges. Filled circles (●) and solid lines connecting two filled circles are a single phase. Small letters (a to f) in the diagram represent a chemical composition as in the right of this figure. *Source*: Adapted from [16]

Region (2)

The $InAlO_3$–ZnO system contains $InAlO_3(ZnO)_m$ ($m \geq 9$). Unlike $InGaO_3(ZnO)_m$ and $InFeO_3(ZnO)_m$, single-phase $InAlO_3(ZnO)_m$ at 1350°C has not been confirmed for $m < 9$, but has been confirmed for large m (up to $m = 21$).

Region (3)

In the In_2O_3–$ZnAl_2O_4$–ZnO system, solid solutions form in the range $In_2O_3(ZnO)_m$ to $In_{1+x}Al_{1-x}O_3(ZnO)_m$ ($0 < x \leq 1$, $2 \leq m \leq 8$). $InAlO_3(ZnO)_m$ has been confirmed in the range $9 \leq m \leq 21$, and solid solutions form in the range $In_2O_3(ZnO)_m$ to $InAlO_3(ZnO)_m$. When the aluminum composition ratio is higher than that of $InAlO_3(ZnO)_m$, solid solutions are not formed.

Compared with the solid solutions of the In_2O_3–$ZnGa_2O_4$–ZnO and In_2O_3–$ZnFe_2O_4$–ZnO systems, the solid-solution range of homologous compounds in this system depends heavily on the Al composition ratio.

1.2.4 Other Layered-Structure Compounds

In addition to the above-described $InGaO_3(BO)_m$ (B = Zn, Mg, Cu, and Co) and $InAO_3(ZnO)_m$ (A = Fe and Al) [14, 16], various isostructural layered-structure compounds in the R_2O_3–A_2O_3–BO system have been synthesized at various temperatures, where R is a rare-earth element and A is Ga, Fe, or Al [8, 11]. $ScAO_3(ZnO)_m$, where A is Ga, Fe, or Al, was synthesized in the range m = 1–9. $ScAlO_3(BO)_m$ (B = Mg and Mn) have been synthesized up to $m = 3$. In the system In_2O_3–TiO_2–ZnO, which contains Ti^{4+}, the homologous compounds are expressed as $In_{1+x}\left(Ti_{1/2}Zn_{1/2}\right)_{1-x}O_3(ZnO)_m$ (m = 1, 2, 3, 4, and 5, $0 < x < 1$) [54]. Ti^{4+} and Zn^{2+} occupy the sites of the trivalent cation A in $InAO_3(ZnO)_m$; consequently, their average valence is three.

The In_2O_3–Ga_2O_3–ZnO–SnO_2 system contains Sn^{4+}, which is tetravalent as with Ti^{4+}. In this system, $(In_{1-2x}Sn_xZn_x)\ GaO_3(ZnO)_m\ (m = 1,\ 2)$ was synthesized, a solid solution of Sn in $InGaO_3(ZnO)_m$ [55]. This compound substitutes Sn^{4+} and Zn^{2+} for two In^{3+} to retain an average charge of +3 at In^{3+} sites.

Some of the sulfides, selenides, and carbonitrides are also reported to be isostructural with $InGaO_3(ZnO)_m$. Layered-structure sulfides and selenides are characterized by metal and chalcogen elements on their triangular lattices, as with $InGaO_3(ZnO)_m$. The cations occupy the sites with 6- and 4-fold coordination, whereas the cations of $RAO_3(BO)_m$ have 4-, 5-, and 6-fold coordination. An adjacent plane perpendicular to the c-axis lies between the chalcogen elements. As the chemical bonds between the planes are extremely weak, the planes between adjacent chalcogen elements are more easily cleaved than the planes between adjacent oxygen elements. The In_2S_3–ZnS and $InGaS_3$–ZnS systems include $(In_2S_3)_n(ZnS)_m$, $InGaS_3(ZnS)_m$, and several polytypes of these [27]. The Al_4C_3–AlN system contains aluminum carbonitrides with composition $Al_4C_3(AlN)_m$ and crystal structures similar to that of $InGaO_3(ZnO)_m$ [25, 26]. Note that Al^{3+}, C^{4-}, and N^{3-} exist in the atomic coordination of O^{2-}, trivalent cations, and divalent cations, respectively.

1.3 Crystal Structures

In 1975, French and Japanese researchers independently determined the crystal structure of $YbFe_2O_4$ and $(Eu_{0.5}Fe_{0.5})Fe_2O_4$, which are isostructural with $InGaO_3(ZnO)$, by single-crystal X-ray diffraction. Subsequently, the single-crystal structures of YFe_2O_4, $InAlCuO_4$, $LuFe_2O_4$, and $InGaZnO_4$, which are isostructural with $YbFe_2O_4$ and $(Eu_{0.5}Fe_{0.5})Fe_2O_4$, were reported. The history of these discoveries is summarized in Table 1.3. YFe_2O_4 and $LuFe_2O_4$ under controlled oxygen partial pressure, and $LuFeMgO_4$ and $YbFeCoO_4$ under atmospheric pressure, were synthesized by the floating-zone method. $InGaO_3(ZnO)$ was synthesized as a powder in 1985, and single crystals of this compound were synthesized under high pressure (2 GPa) and subsequently under atmospheric pressure.

Table 1.3 Analyses of $YbFe_2O_4$-type structures, listed in chronological order

RABO_4-type	Year	Sample of structure analysis	Reference
$YbFe_2O_4$	1975	single crystal	[18]
$(Eu_{0.5}Yb_{0.5})Fe_2O_4$	1975	single crystal	[56]
YFe_2O_4	1976	single crystal	[19]
$InAlCuO_4$	1980	single crystal	[57]
$InGaZnO_4$	1985	powder	[8]
$LuFe_2O_4$	1990	single crystal	[20, 58]
$LuFeCoO_4$	1990	single crystal	[20, 58]
$YbFeMgO_4$	1990	single crystal	[20]
$LuFeZnO_4$	1994	single crystal	[22]
$ErFeZnO_4$	2000	single crystal	[59]
$InGaZnO_4$	2000	single crystal (under high pressure)	[60]
$InGaZnO_4$	2014	single crystal	[61]

1.3.1 Crystal Structures of $InGaO_3(ZnO)_m$ (m = 1, 2, 3, and 4)

1.3.1.1 Crystal Structure of $InGaO_3(ZnO)$

The crystal structure of $InGaO_3(ZnO)$ was revealed by structural analysis of its powder [8] and single crystals [60]. The crystals synthesized by Nespolo *et al.* [60] were sufficiently large for single-crystal structure analysis. As for the synthesis method, they conducted a solid-state reaction of In_2O_3, Ga_2O_3, and ZnO powders in a platinum tube. These were synthesized in the tube under a pressure of 2 GPa at 1200°C for 20 h. Assenmacher *et al.* [61] grew single crystals by the solid-state reaction method under atmospheric pressure, and synthesized $InGaZnO_4$ with a defect structure (Figure 1.9). Their synthesis conditions were at 1550°C for 6 days in a platinum tube.

$InGaO_3(ZnO)$ is isostructural with $YbFe_2O_4$, and forms a rhombohedral lattice with space group $R\bar{3}m$ and 7 atoms per primitive cell (21 atoms in the conventional hexagonal cell). Hereafter in this book we choose the hexagonal cell to represent the Bravais lattice, instead of a rhombohedral cell. The structural parameters for $YbFe_2O_4$ determined by Kato are shown in Tables 1.4 and 1.6, and the parameters for $InGaO_3(ZnO)$ determined by Nespolo are shown in Tables 1.4–1.6. Based on these parameters, the crystal structure model in Figure 1.10 was constructed. O^{2-} forms a two-dimensional close-packed structure (technically called a "eutactic[2] structure"), and the oxygen planes are perpendicular to the *c*-axis in the hexagonal crystal system.

[2] We should explain here the term "eutactic structure," which might be unfamiliar to many readers. In ionic structures, anions conventionally form close-packed structures whose voids are filled with aligned cations. To minimize the repulsive Coulomb interaction, the anions maximize their separation from other anions. In some crystals such as BaO, the anions are scarcely larger than the cations (see ionic radii of Shannon crystals [24]). At the optimal cation–anion distance in the ionic structure, the crystal structure with the dominant electrostatic energy is similar to the close-packed arrangement. O'Keeffe [62] proposed the term "eutactic," derived from the noun "eutaxy" (good arrangement), as a simple description of this crystal arrangement.

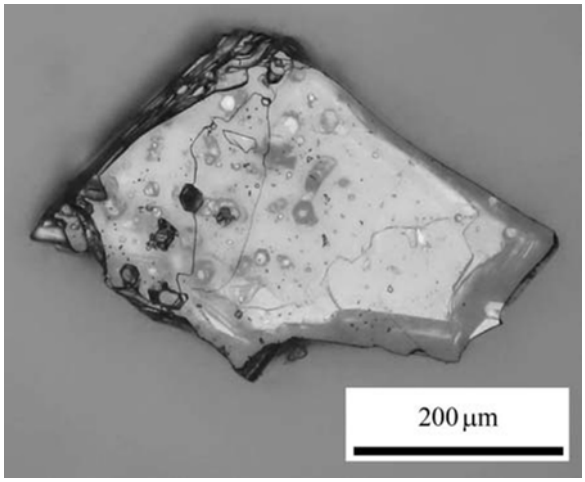

Figure 1.9 Optical micrograph of an $InGaO_3(ZnO)$ crystal. To our knowledge, this is one of the largest single crystals of $InGaZnO_4$ ever reported. *Source*: Reprinted from [61], Copyright (2014), with permission from Elsevier

Table 1.4 Atomic coordinates of $InGaO_3(ZnO)$ and $YbFe_2O_4$. *Source*: Adapted from [18, 60]

Element	Label	Wyckoff position	Site occupancy factor	Fractional coordinates within the unit cell		
				x	*y*	*z*
			$InGaO_3(ZnO)$			
In	In1	3*a*	1	0.00000	0.00000	0.00000
Ga	*M*1	6*c*	0.5	0.00000	0.00000	0.2171(1)
Zn	*M*1	6*c*	0.5	0.00000	0.00000	0.2171(1)
O	O1	6*c*	1	0.00000	0.00000	0.2928(1)
O	O2	6*c*	1	0.00000	0.00000	0.1282(1)
			$YbFe_2O_4$			
Yb	Yb1	3*a*	1	0.00000	0.00000	0.00000
Fe	Fe1	6*c*	1	0.00000	0.00000	0.2150(1)
O	O1	6*c*	1	0.00000	0.00000	0.2925(3)
O	O2	6*c*	1	0.00000	0.00000	0.1292(5)

Table 1.5 Bond lengths [nm] and angles [°] of $InGaO_3(ZnO)$. *Source*: Adapted from [60]

		*M*1	*M*1	In1	O2
Bond length [nm]	O1	0.1976			0.2977
	O2	0.1930	0.2320	0.2178	
Angle [°]		∠(O1–In1–O1)		98.414	
		∠(O1–*M*1–O2)		99.313	
		∠(O2–*M*1–O2)		117.434	

Table 1.6 Crystal data of $YbFe_2O_4$ and $InGaO_3(ZnO)$. *Source*: Adapted from [18, 60]

Formula	$InGaZnO_4$	$YbFe_2O_4$
Space group	$R\bar{3}m$ (No. 166)	
Cell constant a [nm]	0.3299	0.3455
Cell constant c [nm]	2.6101	2.505
Calculated density [g/cm^3]	6.357	6.707

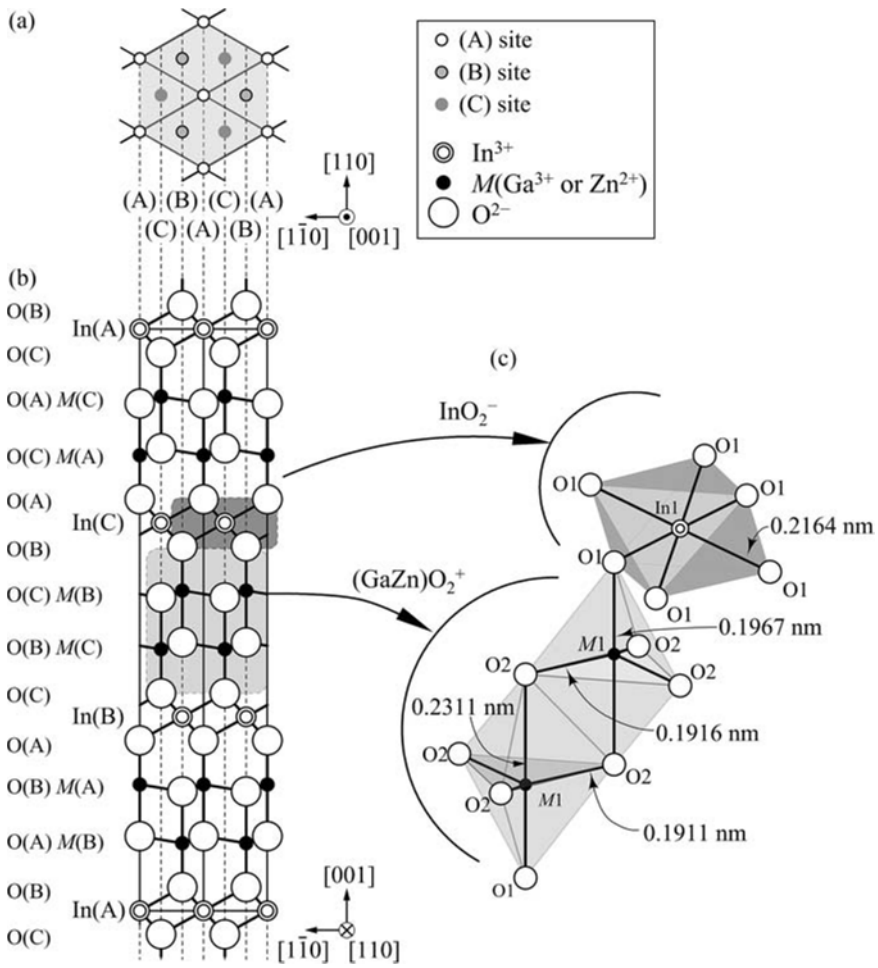

Figure 1.10 Structure of $InGaO_3(ZnO)$ projected onto (a) the (001) plane and (b) the (110) plane. (c) A bird's-eye view of coordination of the cations (In, Ga, Zn) in $InGaO_3(ZnO)$. Small double-open circles, small filled circles, and large open circles denote In, *M* (Ga or Zn), and O atoms, respectively. In (a), (*X*) signifies site *X* [e.g., (A) = site A]. In (b), In(*X*), *M*(*X*), and O(*X*) denote In^{3+}, a cation (Ga^{3+} or Zn^{2+}), and O^{2-} that occupy site (*X*), respectively. For example, In(A) = In^{3+} that occupies site A. In (c), symbols (e.g., O1 and *M*1) are labels of elements that lie on an equivalent position, as listed in Table 1.4. *Source*: Adapted from [60]

Figure 1.10 shows the atomic structure of $InGaO_3(ZnO)$. All of the cations and anions lie on the triangular lattices. The In^{3+} cations occupy the 6-fold site surrounded by a distorted O^{2-} octahedron. The octahedrons share their edges and are connected parallel to the (001) plane of the hexagonal cell. The layered structure is identical to the CdI_2-type structure (hexagonal, $P\bar{3}m1$) and is described as an InO_2^- unit. Ga^{3+} and Zn^{2+} occupy the 5-fold site surrounded by an O^{2-} trigonal bipyramid, which is off the common base plane of two trigonal bipyramids. The trigonal bipyramids also share edges and are connected parallel to the (001) plane of the hexagonal cell. The two layers of the trigonal bipyramids are parallel to the *c*-axis and are stacked with shared edges. Collectively, these layers are referred to as a $(GaZn)O_2^+$ unit. This unit is not perfectly isostructural with wurtzite-type structures, but its motif in the $(GaZn)O_2^+$ unit has a wurtzite-type structure. Four of the five bonds between the O_2^- and cations (Ga^{3+} and Zn^{2+}) are less than 0.2 nm, and the maximum length of the longest bond (the cation–anion bond) is 0.2311 nm. From the structural perspective of a $(GaZn)O_2^+$ unit, the bases face each other. Each tetrahedron is similar to a wurtzite-type structure; in the basic structure, the layers of the two local parts [InO_2^- and $(GaZn)O_2^+$ units] are alternately stacked. These layers connect by sharing their vertexes and are arranged in triple layers along the *c*-axis of the unit cell.

In the $InGaO_3(ZnO)$ structure, the cations (In^{3+}, Ga^{3+}, and Zn^{2+}) and anions (O_2^-) lie on the triangular lattices as viewed from the *c*-axis direction. Figure 1.11 shows the alignment of the cations and anions on the triangular lattices. In the unit cell, they are aligned on any of the three sites labeled A, B, and C in the figure. In the InO_2^- unit, In^{3+}, O^{2-} above In_3^+, and O^{2-} beneath In^{3+} occupy different sites (e.g., A, B, and C, respectively). In the $(GaZn)O_2^+$ unit likewise, Ga^{3+}, Zn^{2+}, and O^{2-} occupy different A–C sites. Below, we consider the cations and anions occupying the sites in each layer. The stacking sequence (i)–(v) in Figure 1.11 is explained as follows.

i. Assume that site A is occupied by In^{3+} with 6-fold coordination. Each anion above and beneath In^{3+} lies on a triangular lattice that is offset from the cation sites. An example of this alignment is O(C)–*M*(A)–O(B), which denotes that O^{2-}, a cation (In^{3+}), and O^{2-} occupy sites C, A, and B, respectively [as shown in Figure 1.11(a)]. This represents a combination of an element and a site projected onto the (001) plane.
ii. The layer formed in (i) is topped by a layer with the same number of cations and anions. Cations occupy the anion sites in the lower layer (site B), whereas O^{2-} occupy site A, because this arrangement minimizes the distance between the cations and anions in the ionic crystal.
iii. Likewise, the above-mentioned layer is topped by a layer with the cations and anions occupying the A and B sites, respectively. The number of layers sandwiched by InO_2^- depends on *m* in $InGaO_3(ZnO)_m$. When $m = 1$, the two layers (that is, the $GaZnO_2^+$ unit) are sandwiched by InO_2^- units; hereafter we consider the case of $m = 1$. When $m = 3, 5, \ldots$, the number of layers inserted between the InO_2^- unit is two, four, …, respectively. If two layers are inserted in $(GaZn_m)O_{m+1}$, the cations and anions in the lower inserted layer are located at the B sites and A sites, respectively, whereas the cations and anions in the upper inserted layer are located at the A sites and B sites. Therefore, the arrangement of cations and anions at the top layer in the $(GaZn_m)O_{m+1}$ unit is the same if an even number of layers is inserted in the $(GaZn_m)O_{m+1}$ unit.
iv. The anions in the InO_2^- unit are aligned over the lower layer and occupy the same positions as the lower cations (site A).

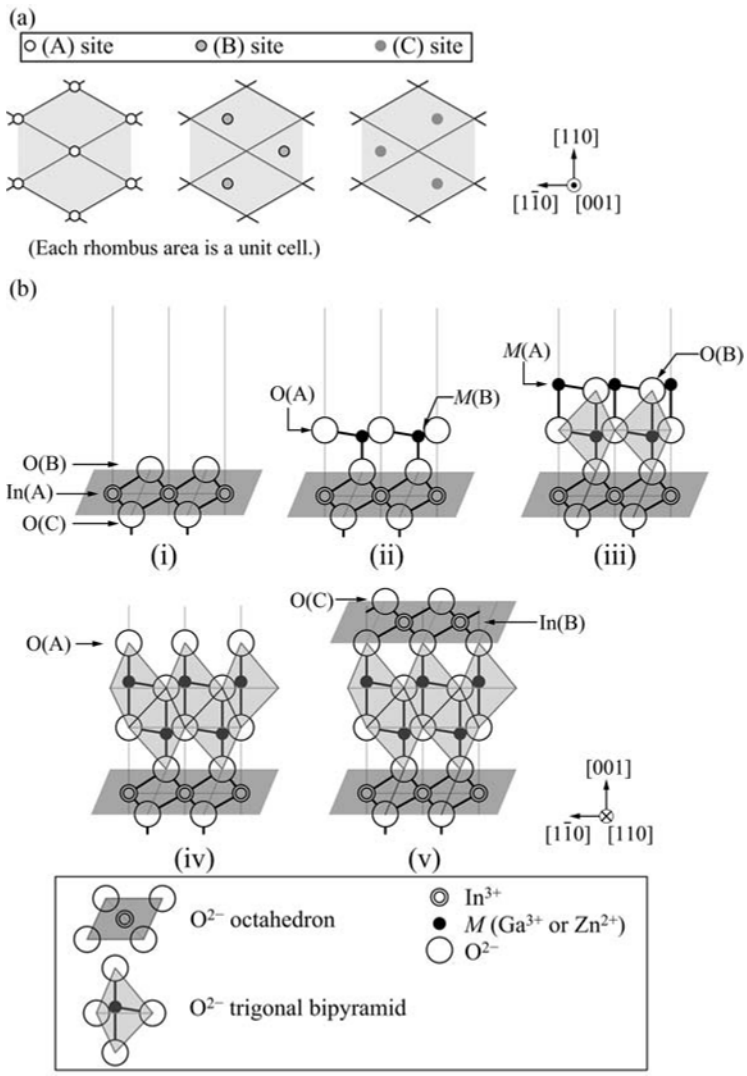

Figure 1.11 (a) Sites in the hexagonal lattice projected onto the (001) plane. (b) Stacking sequence (i)–(v) in the $InGaO_3(ZnO)$ structure projected onto the (110) plane. In, *M* (Ga or Zn), and O atoms are indicated by small double-open circles, small filled circles, and large open circles, respectively

v. As seen above, site B is filled with cations in 6-fold coordination, thus minimizing the anion–cation distance. This alignment is site-B-centered, or O(A)–*M*(B)–O(C). At this stage, no unit cell of hexagonal representation is formed because the In^{3+} is shifted from the initial A sites. If the site-B-centered InO_2^- unit (6-fold coordination) is now regarded as the initial state, and the cations and anions are aligned by the same methods, then the next 6-fold coordinate cations in the InO_2^- unit fill the C sites, and the subsequent ones return to the A sites. Hence, when *m* is odd, the unit cell of the hexagonal representation contains three InO_2^- units.

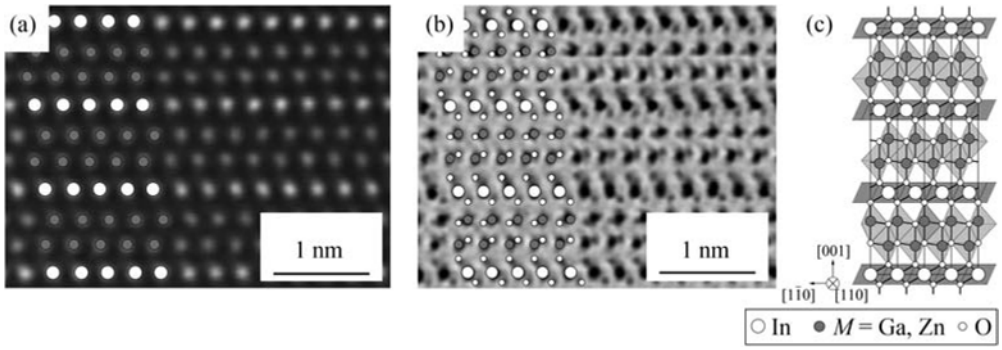

Figure 1.12 (a) HAADF-STEM image and (b) ABF-STEM image of $InGaO_3(ZnO)$ projected onto the (110) plane. Higher contrast indicates elements with higher atomic number. In (c), In, Ga and/or Zn, and O atoms are indicated schematically by large open circles, gray circles, and small open circles, respectively

In summary, the O^{2-} packing along the *c*-axis alters as follows (Figure 1.10):

1. CBCB to ACAC, bordered by indium in an InO_2^- unit of site C;
2. BABA to CBCB, bordered by indium in an InO_2^- unit of site B;
3. ACAC to BABA, bordered by indium in an InO_2^- unit of site A.

Meanwhile, the cation packing along the *c*-axis alters as follows (Figure 1.10):

1. CB to AC, bordered by indium in an InO_2^- unit of site C;
2. BA to CB, bordered by indium in an InO_2^- unit of site B;
3. AC to BA, bordered by indium in an InO_2^- unit of site A.

Figure 1.12(a) and (b) shows a HAADF-STEM image and ABF-STEM image of layered-structure $InGaO_3(ZnO)$, respectively (for details, see Appendix 1.A.2.1). In the HAADF-STEM image, heavy elements are clearly visible because the contrast increases with increasing atomic number of the constituent elements, whereas in the ABF-STEM image, columns of light elements can be observed effectively.

Figure 1.12(a) exhibits one layer with strong contrast (the indium layer) and two layers with relatively weak contrast (gallium or zinc layers). Because the atomic numbers of Ga and Zn are very close (31 and 30, respectively), the two elements cannot be distinguished in this image. However, the alternate stacking of the InO_2^- and $(GaZn)O_2^+$ units in the $InGaO_3(ZnO)$ crystal is clearly visible. Figure 1.12(b) exhibits columns of oxygen above and below columns of cation, as shown schematically in Figure 1.12(c).

1.3.1.2 Crystal Structure of $InGaO_3(ZnO)_m$ (m = 2, 3, 4)

The crystal structure of $InGaO_3(ZnO)_m$ (m = 2, 3, 4) was revealed by analyses of its powder [11, 12] and single crystals (except m = 3) [23, 63, 64]. Keller *et al*. [63, 64] grew single crystals in

a flux of K_2MoO_4. They heated potassium molybdate and mixed powders of In_2O_3, Ga_2O_3, and ZnO in a sealed platinum tube at 1350°C for 5 days.

This section elucidates the crystal structure of $InGaO_3(ZnO)_m$ (m = 2, 3, 4) from crystal structure analysis data [63, 64]. $InGaO_3(ZnO)_2$ is a hexagonal lattice with space group $P6_3/mmc$ and contains 18 atoms per primitive hexagonal cell. The structural parameters for $InGaO_3(ZnO)_2$ determined by Keller are shown in Tables 1.7 and 1.8. Based on these parameters, the crystal structure model was constructed as shown in Figure 1.13.

O^{2-} forms a two-dimensional close-packed structure (eutactic structure), with the oxygen planes perpendicular to the c-axis in the hexagonal crystal system. In each InO_2^- layer, the octahedrons share their edges and are connected perpendicular to the c-axis. Ga^{3+} and Zn^{2+} fill the 5-fold coordination sites surrounded by O^{2-} trigonal bipyramids or O^{2-} tetrahedrons. Keller *et al*. assumed that the 4- and 5-fold oxygen coordination sites are occupied by Zn^{2+} and Ga^{3+} ions, respectively. In this book, we adopt the same assumption.

The Ga^{3+} and Zn^{2+} cations in the trigonal-bipyramid sites locate on the base plane shared by the trigonal pyramids. In other words, the cations lie in the base plane composed by the

Table 1.7 Atomic coordinates and isotropic displacement parameters of $InGaO_3(ZnO)_2$. *Source*: Reprinted from [63], Copyright (2009), with permission from Wiley

Element	Label	Wyckoff position	Site occupancy factor	x	y	z	U [Å^2]
In	In1	24	1	0.00000	0.00000	0.00000	0.0059(2)
Zn	Zn1	4*f*	1	0.66667	0.33333	0.36538(5)	0.0051(3)
Ga	Ga1	2*b*	1	0.00000	0.00000	0.25000	0.0061(3)
O	O1	4*f*	1	0.66667	0.33333	0.4525(3)	0.006(1)
O	O2	4*e*	1	1.00000	0.00000	0.3451(3)	0.010(1)
O	O3	2*d*	1	–0.33333	0.33333	0.25000	0.016(2)

Table 1.8 Bond lengths [nm] and angles [°] of $InGaO_3(ZnO)_2$. *Source*: Reprinted from [63], Copyright (2009), with permission from Wiley

		Ga1	In1	Zn1	O2	O3
Bond length [nm]	O1	0.4933	0.2180	0.1958	0.3073	0.4553
	O2	0.2137	0.3483	0.1954		0.2855
	O3	0.1900	0.5934	0.2594		
Angle [°]		∠(O2–Ga1–O3)		90.000		
		∠(O3–Ga1–O3)		120.000		
		∠(O1–In1–O1)		98.027		
		∠(O1–Zn1–O2)		103.507		
		∠(O2–Zn1–O2)		114.719		

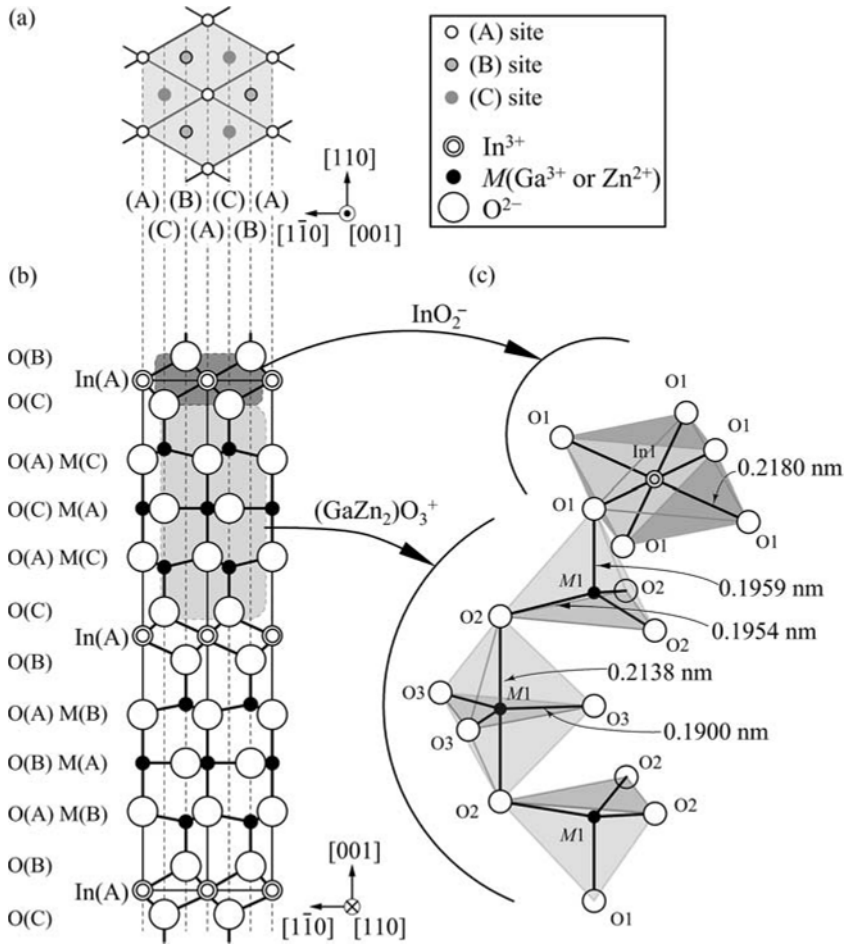

Figure 1.13 Structure of $InGaO_3(ZnO)_2$ projected onto (a) the (001) plane and (b) the (110) plane. (c) A bird's-eye view of coordination of the cations (In, Ga, Zn) in $InGaO_3(ZnO)_2$. Small double-open circle, small filled circles, and large open circles denote In, *M* (Ga or Zn), and O atoms, respectively. In (a), (*X*) signifies site *X* [e.g., (A) = site A]. In (b), In(*X*), *M*(*X*), and O(*X*) denote In^{3+}, a cation (Ga^{3+} or Zn^{2+}), and O^{2-} that occupy site (*X*), respectively. For example, In(A) = In^{3+} that occupies site A. In (c), symbols (e.g., O1 and *M*1) are labels of elements that lie on an equivalent position, as listed in Table 1.7. *Source*: Adapted from [63]

three O_2^- ions. The trigonal bipyramids share their vertexes perpendicular to the *c*-axis of the hexagonal lattice, and form a layer between the InO_2^- units. The tetrahedrons also share their vertexes perpendicular to the *c*-axis of the hexagonal lattice, and their 4-fold oxygen coordinated sites are filled with cations. $InGaO_3(ZnO)_2$ has two layers of tetrahedral sites between its InO_2^- units. Thus, along the *c*-axis, the shared vertexes of the tetrahedral sites are alternated with bipyramid sites. In other words, the layer sequence is (InO_2^-)-{(4-fold site)-(5-fold site)-(4-fold site)}-(InO_2^-). $(GaZn_2)O_3^+$ comprises three layers of continuous trigonal

bipyramids and tetrahedrons. In the $(GaZn_2)O_3^+$ unit, the tetrahedrons invert from the trigonal-bipyramid layer and closely resemble a wurtzite-type structure. The basic structure is an alternate stacking of two local units (InO_2^- and $(GaZn_2)O_3^+$). The layers connect by sharing their vertexes. Thus, $InGaO_3(ZnO)$ is constructed from three repeats of two types of layers, whereas the unit cell of $InGaO_3(ZnO)_2$ is constructed from twice-repeated InO_2^- and $(GaZn_2)O_3^+$ layers along the *c*-axis.

The cations (In^{3+}, Ga^{3+}, and Zn^{2+}) and anions (O^{2-}) in $InGaO_3(ZnO)_2$ are arranged in a triangular formation when viewed along the *c*-axis. The cation and anion alignments on the triangular lattice are shown in Figure 1.14. In the unit cell, the cations and anions fill any of the sites labeled A, B, and C in the figure, which lie on the triangular lattice. We now consider which sites are occupied by cations and anions in each layer. The stacking sequence (i)–(v) in Figure 1.14 is explained as follows.

i. Assume that the A sites are occupied by cations with InO_2^-. Each anion arrayed above and below the cations occupies a triangular lattice that differs from the cation sites. This alignment is formally expressed as $O(C)-M(A)-O(B)$. As mentioned in Subsection 1.3.1.1, this represents a combination of an element and a site projected onto the (001) plane.
ii. This layer is topped by a layer with the same number of cations (Ga^{3+} and Zn^{2+}) and anions (O^{2-}). The cations in this layer occupy the B site, which is on top of the lower InO_2^- unit. In contrast, the oxygens occupy the A site, which is the In^{3+} site of the lower InO_2^- unit, because this arrangement minimizes the distance between the cations and anions.
iii. If the layer in (ii) is topped by another layer, the metals and anions occupy the A and B sites, respectively. The number of layers depends on *m*; here we consider the case $m = 2$.
iv. When $m = 2$, the $(GaZn_2)O_3^+$ are sandwiched between InO_2^- units, so that we add another layer above to (ii) and (iii). In this layer, the cations and anions locate at the B sites (occupied by anions in the lower level) and the A sites (occupied by cations in the lower level), respectively. When $m = 4, 6, \ldots$, the number of layers inserted between InO_2^- units is two, four, …, respectively. If two layers are inserted ($m = 4$), the cations and anions in the lower inserted layer are located at the A sites and B sites. Likewise, the cations and anions in the upper inserted layer are located at the B sites and A sites. Therefore, the arrangement of cations and anions in the top layer is the same if even numbers of layer units are inserted.
v. Above layer (iv), the anions which will become the bottom of the InO_2^- unit occupy the same sites as the lower cations (site B). Next, the In^{3+} in the InO_2^- unit occupy the A sites, to minimize their distance from attractive anions in the same way as (ii). Therefore, the arrangement is site-A-centered, or $O(B)-M(A)-O(C)$. Beginning with the InO_2^- unit, we obtain the same In^{3+} site arrangement, but here the anion arrangement is inverted. Unlike the $m = 1$ case, the In sites are not shifted; rather, merely exchanging B and C generates the correct arrangement. The arrangement in the next InO_2^- unit is $O(C)-M(A)-O(B)$ (because the O sites are inverted again); therefore, when *m* is even, the unit cell of the hexagonal representation contains two InO_2^- units.

In summary, the O^{2-} and cation packing along the *c*-axis changes from BABAB to CACAC and from BAB to CAC, respectively. Both alternations are bordered by indium in the InO_2^- layer of the A sites (Figure 1.14).

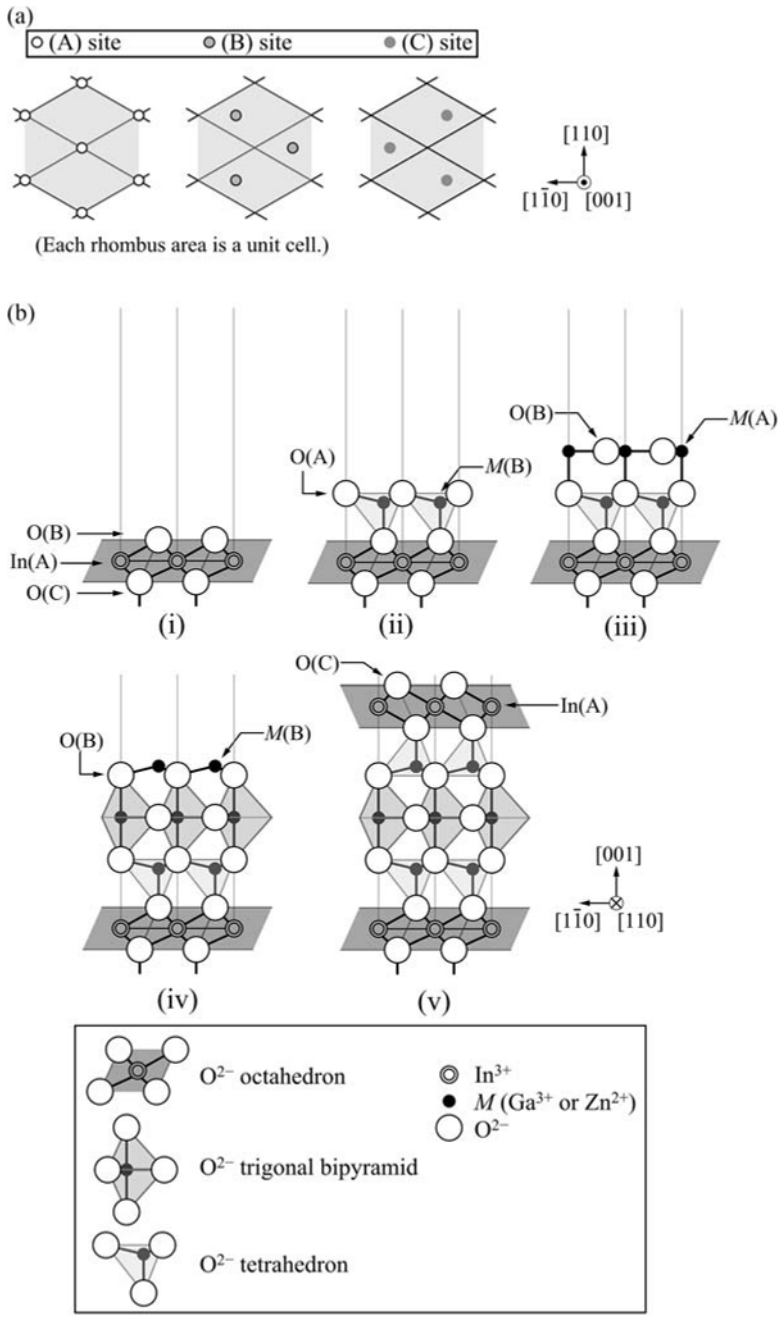

Figure 1.14 (a) Sites in the hexagonal lattice projected onto the (001) plane. (b) Stacking sequence in the $InGaO_3(ZnO)_2$ structure projected onto the (110) plane. Small double-open circles, small filled circles, and open circles denote In, *M* (Ga or Zn), and O atoms, respectively

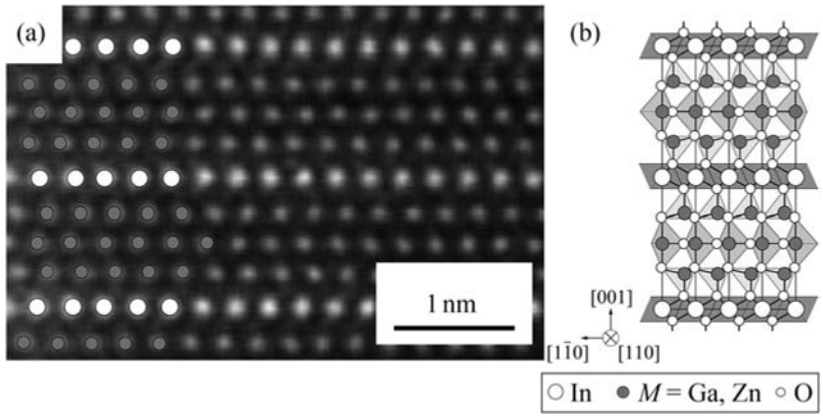

Figure 1.15 HAADF-STEM image of the $InGaO_3(ZnO)_2$ phase in the system In_2O_3–Ga_2O_3–ZnO, projected onto the (110) plane. Higher contrast indicates elements with higher atomic number. In the right-hand schematic, the In, Ga, and/or Zn and O atoms are denoted by large open circles, gray circles, and small filled circles, respectively

Table 1.9 Atomic coordinates and isotropic displacement parameters of $InGaO_3(ZnO)_3$. *Source*: Reprinted from [63], Copyright (2009), with permission from Wiley

Element	Label	Wyckoff position	Site occupancy factor	x	y	z	U [Å^2]
In	In1	3*a*	1	0.00000	0.00000	0.00000	0.0303(3)
Zn	Zn1	6*c*	1	0.00000	0.00000	0.73956(9)	0.0274(2)
Ga	*M*2	6*c*	0.5	0.00000	0.00000	0.13539(9)	0.0297(0)
Zn	*M*2	6*c*	0.5	0.00000	0.00000	0.13539(9)	0.0297(3)
O	O1	6*c*	1	0.00000	0.00000	0.3061(4)	0.04(2)
O	O2	6*c*	1	0.00000	0.00000	0.0864(3)	0.006(6)
O	O3	6*c*	1	0.00000	0.00000	0.8071(3)	0.019(0)

Figure 1.15 is a HAADF-STEM image (Appendix 1.A.2.1) of the layered-structure $InGaO_3(ZnO)_2$ phase. One layer exhibits strong contrast (indicating indium, an element with a relatively high atomic number); the remaining three layers show relatively weak contrast (indicating gallium or zinc, both with lower atomic numbers). Clearly, the InO_2^- and $(GaZn_2)O_3^+$ units are alternately stacked in the $InGaO_3(ZnO)_2$ crystal.

$InGaO_3(ZnO)_3$ is a rhombohedral lattice with space group $R\bar{3}m$ and contains 33 atoms per conventional hexagonal cell. Tables 1.9 and 1.10 list the $InGaO_3(ZnO)_3$ structural parameters determined by Keller. The crystal structure model derived from these parameters is presented in

Table 1.10 Bond lengths [nm] and angles [°] of $InGaO_3(ZnO)_3$. *Source*: Adapted from [63]

		In1	Zn1	Ga2/Zn2	O2	O3
Bond length [nm]	O1	0.2211	0.1899	0.4883	0.3108	0.4708
	O2	0.3593	0.1981	0.2037		0.2942
	O3	0.8023	0.5340	0.2392		
Angles [°]		∠(O2–Ga2/Zn2–O3)		96.302		
		∠(O3–Ga2/Zn2–O3)		118.811		
		∠(O1–In1–O1)		96.115		
		∠(O1–Zn1–O2)		106.476		
		∠(O2–Zn1–O2)		112.293		

Figure 1.16. $InGaO_3(ZnO)_3$ has the composition of $InGaO_3(ZnO)_2$ with an additional ZnO layer. Specifically, it is structured similarly to $InGaO_3(ZnO)$, but has a tetrahedral layer of wurtzite-type ZnO above and below the $(GaZn)O_2^+$ unit of $InGaO_3(ZnO)$. The four layers with continuous trigonal bipyramids and tetrahedrons constitute a $(GaZn_3)O_4^+$ unit. The $(GaZn_3)O_4^+$ stacking sequence is (InO_2^-)-{(4-fold site)-(5-fold site)-(5-fold site)-(4-fold site)}-(InO_2^-). The basic structure comprises three repeats of the InO_2^- and $(GaZn_3)O_4^+$ units along the *c*-axis direction.

$InGaO_3(ZnO)_4$ is a hexagonal lattice with space group $P6_3/mmc$, containing 26 atoms per primitive hexagonal cell. Tables 1.11 and 1.12 list the structural parameters of $InGaO_3(ZnO)_4$ determined by Keller, and the derived crystal structure model is shown in Figure 1.17. $InGaO_3(ZnO)_4$ is composed of $InGaO_3(ZnO)_3$ with additional ZnO, and its basic structure is similar to that of $InGaO_3(ZnO)_2$. Above and below the $(GaZn_2)O_3^+$ unit of $InGaO_3(ZnO)_2$, the structure is bounded by a tetrahedral layer of wurtzite-type ZnO, as observed in the structural change from $InGaO_3(ZnO)$ to $InGaO_3(ZnO)_3$. The five layers with continuous trigonal bipyramids and tetrahedrons constitute $(GaZn_4)O_5^+$, which is stacked as (InO_2^-)-{(4-fold site)-(4-fold site)-(5-fold site)-(4-fold site)-(4-fold site)}-(InO_2^-). The basic structure comprises InO_2^- and $(GaZn_4)O_5^+$ units arranged in double layers along the *c*-axis direction.

The crystal structures of the group of compounds formulated as $InGaO_3(ZnO)_m$ depend on whether *m* is even or odd. In $InGaO_3(ZnO)_m$, the 6-fold coordination sites are isostructural with CdI_2-type structures. In the 4- or 5-fold coordination sites, the structure is locally formulated as $(GaZn_m)O_{m+1}^+$, whose structure also depends on *m*. For instance, when $m = 1$, the trigonal bipyramids in $(GaZn_m)O_{m+1}^+$ connect by shared edges; for all higher *m*, the tetrahedrons are stacked with shared vertexes and are vertically adjacent to trigonal bipyramids. As *m* increases or the sites of tetrahedrons approached the InO_2^- unit, the tetrahedrons in the $(GaZn_m)O_{m+1}^+$ unit become similar to those in ZnO.

In the $InGaO_3(ZnO)_m$ series, whether *m* is even or odd affects only the stacking sequence; it does not markedly alter the local structural combinations (Figure 1.18). Therefore, the $InGaO_3(ZnO)_m$ series constitutes a homologous series.

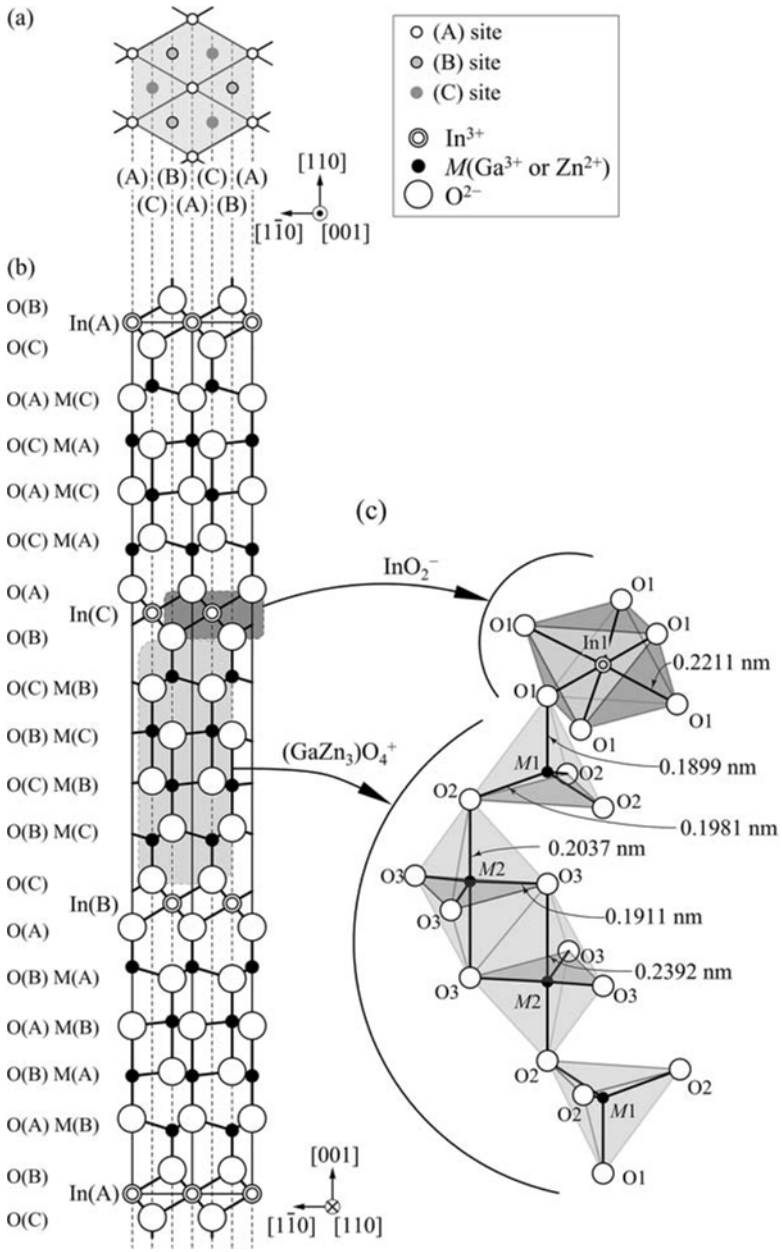

Figure 1.16 Structure of $InGaO_3(ZnO)_3$ projected onto (a) the (001) plane and (b) the (110) plane. (c) A bird's-eye view of coordination of the cations (In, Ga, Zn) in $InGaO_3(ZnO)_3$. Small double-open circles, small filled circles, and large open circles denote In, *M* (Ga or Zn), and O atoms, respectively. In (a), (*X*) signifies site *X* [e.g., (A) = site A]. In (b), In(*X*), *M*(*X*), and O(*X*) denote In^{3+}, a cation (Ga^{3+} or Zn^{2+}), and O^{2-} that occupy site (*X*), respectively. For example, In(A) = In^{3+} that occupies site A. In (c), symbols (e.g., O1 and *M*1) are labels of elements that lie on an equivalent position, as listed in Table 1.9. *Source*: Adapted from [63]

Table 1.11 Atomic coordinates and isotropic displacement parameters of $InGaO_3(ZnO)_4$. *Source*: Reprinted from [64], Copyright (2010), with permission from Wiley

Element	Atom	Wyckoff position	Site occupancy factor	x	y	z	U [Å^2]
In	In1	2*a*	1	0.00000	0.00000	0.00000	0.0199(3)
Zn	Zn1	4*f*	1	0.66667	0.33333	0.09218(4)	0.0125(3)
Zn	Zn2	4*e*	1	0.00000	0.00000	0.17122(5)	0.0136(4)
Ga	Ga1	2*d*	1	0.66667	0.33333	0.25000	0.0145(4)
O	O1	4*f*	1	0.66667	0.33333	0.0327(3)	0.013(2)
O	O2	4*e*	1	0.00000	0.00000	0.1092(3)	0.014(2)
O	O3	4*f*	1	0.66667	0.33333	0.1832(4)	0.019(2)
O	O4	2*b*	1	0.00000	0.00000	0.25000	0.037(6)

Table 1.12 Bond lengths [nm] and angles [°] of $InGaO_3(ZnO)_4$. *Source*: Reprinted from [64], Copyright (2010), with permission from Wiley

		In1	Zn1	Zn2	Ga1
Bond length [nm]	O1	0.2181	0.1955		
	O2		0.1978	0.2038	
	O3			0.1937	0.219(1)
	O4				0.1897
Angles [°]		∠(O2–Ga2/Zn2–O3)		96.302	
		∠(O3–Ga2/Zn2–O3)		118.811	
		∠(O1–In1–O1)		96.115	
		∠(O1–Zn1–O2)		106.476	
		∠(O2–Zn1–O2)		112.293	

Above we outlined the layered structures of the series with general formula $InGaO_3(ZnO)_m$ (m = integer), which are listed in Tables 1.13 and 1.14. Meanwhile, whether the Ga and Zn distribution is ordered has been theoretically discussed but not in any conclusive way. From an ionic valence and coordination number perspective, the sum of the bond valences indicates that Zn and Ga are preferred for tetrahedral and trigonal-bipyramid sites, respectively [63, 64]. On the other hand, according to an exploration of the Ga-stable arrangement in an *ab initio* electronic state calculation, a modulated boundary structure is energetically more favorable [65, 66].

1.3.2 Lattice Constants of $InAO_3(ZnO)_m$ (A = In, Fe, Ga, and Al)

As described above, the In_2O_3–Ga_2O_3–ZnO system includes $InGaO_3(ZnO)_m$. The crystal structure of this series comprises stacked layers of polyhedrons such as octahedrons, tetrahedrons, and trigonal bipyramids. As observed in the In_2O_3–Ga_2O_3–ZnO system, substituting Fe or Al

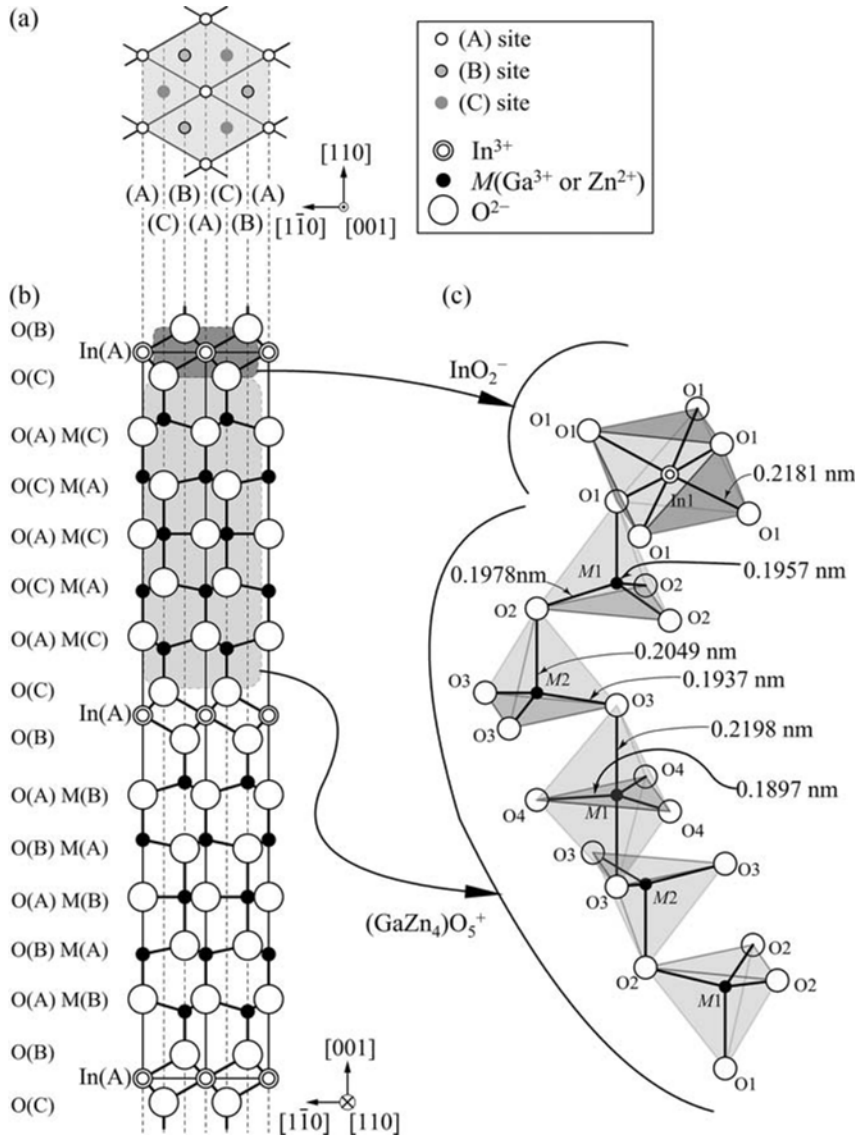

Figure 1.17 Structure of $InGaO_3(ZnO)_4$ projected onto (a) the (001) plane and (b) the (110) plane. (c) A bird's-eye view of coordination of cations (In, Ga, Zn) in $InGaO_3(ZnO)_4$. Small double-open circle, small filled circles, and large open circles denote In, *M* (Ga or Zn), and O atoms, respectively. In (a), (*X*) signifies site *X* [e.g., (A) = site A]. In (b), In(*X*), *M*(*X*), and O(*X*) denote In^{3+}, a cation (Ga^{3+} or Zn^{2+}), and O^{2-} that occupy site (*X*), respectively. For example, In(A) = In^{3+} that occupies site A. In (c), symbols (e.g., O1 and *M*1) are labels of elements that lie on an equivalent position, as listed in Table 1.11. *Source*: Adapted from [64]

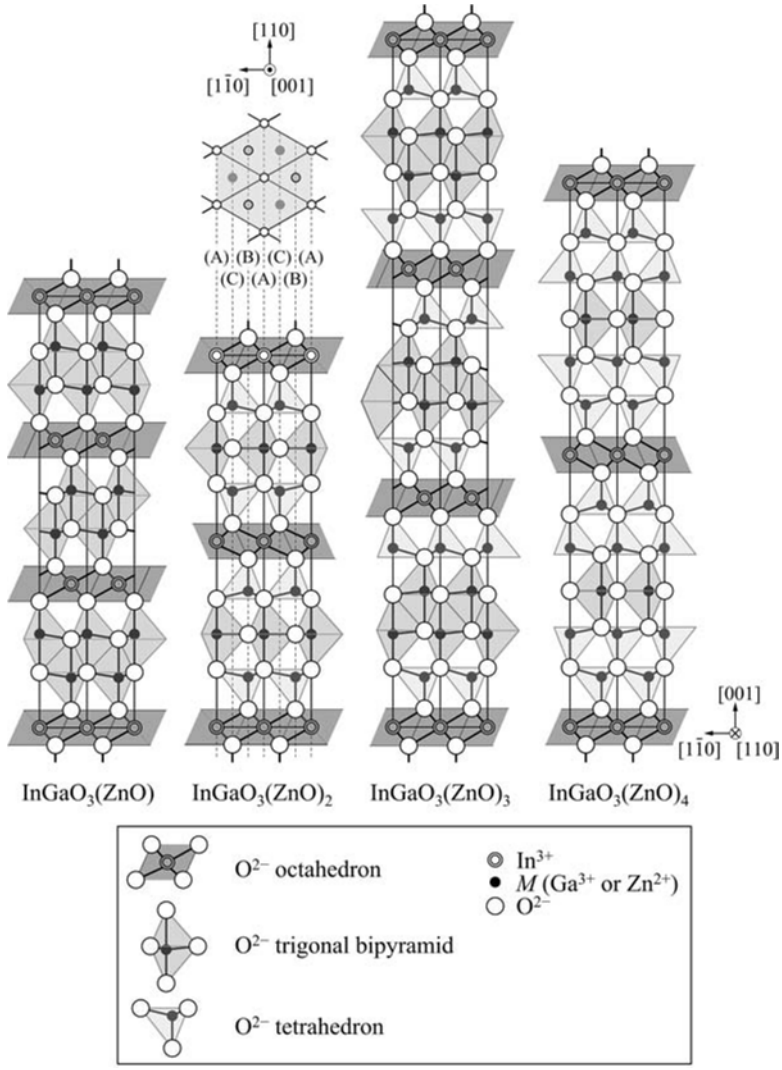

Figure 1.18 Structure of $InGaO_3(ZnO)_m$ ($m = 1$, 2, 3, and 4) projected onto the (001) and the (110) plane. Small double-open circles, small filled circles, and large open circles denote In, *M* (Ga or Zn), and O atoms, respectively. *Source*: Adapted from [60, 63, 64]

for Ga in the ternary oxides does not alter the layered structure. In powder X-ray diffraction analyses, the lattice constants of these crystal structures were determined over a range of *m* from 1 to 20 [12, 67]. From these results, we can elucidate the effect of *m* on the lattice parameters.

To compare the distance between the InO_2^- units along the *c*-axis direction, we divide the lattice constant of the *c*-axis by the repeat number of the InO_2^- units. This approach is justified by the *m*-dependence on the number of InO_2^- units, as described in the previous subsection.

Table 1.13 Crystal data of $InGaO_3(ZnO)_m$ (m: odd number).
Source: Reprinted from [60, 63], with permission from Wiley

Formula	$InGaO_3(ZnO)$	$InGaO_3(ZnO)_3$
Space group	$R\bar{3}m$ (No. 166)	
Cell constant a [nm]	0.3299	0.3290
Cell constant c [nm]	2.6101	4.1589
Calculated density [g/cm^3]	6.36	6.09

Table 1.14 Crystal data of $InGaO_3(ZnO)_m$ (m: even number).
Source: Reprinted from [63, 64], with permission from Wiley

Formula	$InGaO_3(ZnO)_2$	$InGaO_3(ZnO)_4$
Space group	$P6_3/mmc$ (No. 194)	
Cell constant a [nm]	0.3291	0.3285
Cell constant c [nm]	2.2485	3.2906
Calculated density [g/cm^3]	6.225	6.026

Figures 1.19 and 1.20 plot the m-dependence of the lattice parameter a and c/z in hexagonal $InAO_3(ZnO)_m$. The relationship between m and c/z depends on the length of the c-axis [12]. Here, z is the repeat number of InO_2^- and $(GaZn_m)\,O_{m+1}^+$ units in the unit cell, and c/z is the c-axis length corresponding to a pair of InO_2^- and $(GaZn_m)\,O_{m+1}^+$ units. The c/z of odd and even m equals 3 and 2, respectively. The lattice parameter a (in the unit cell of the hexagonal representation) defines the distance between the closest O–O on the (001) plane. As the chemical composition varies from $InGaO_3(ZnO)$ to $InGaO_3(ZnO)_m$ (where m is large), the lattice parameter a approaches that of ZnO as m increases.

The m-dependence can be explained as follows. The closest O–O in the (001) plane corresponds to an edge of a tetrahedron in a $(GaZn_m)O_{m+1}^+$ unit; in the limit of m, the closest O–O in the (001) plane of ZnO similarly corresponds to an edge of a tetrahedron. The tetrahedrons in $(GaZn_m)O_{m+1}^+$ are similar to those of ZnO. As the m of $(GaZn_m)O_{m+1}^+$ increases, the tetrahedrons in $(GaZn_m)O_{m+1}^+$ become more similar to those of ZnO, shortening the closest O–O distance in the (001) plane. In all members of the $InAO_3(ZnO)$–ZnO (A = Ga, Fe, Al) system, the lengths of the a-axis of $InGaO_3(ZnO)_m$ and ZnO converge as m increases.

When the lattice parameter c is normalized by the thickness of a pair of InO_2^- and $(GaZn_m)O_{m+1}^+$ units along the c-axis direction, the c/z increases almost linearly with m, regardless of whether m is even or odd. As m increases by one, the thickness of $(GaZn_m)O_{m+1}^+$ increases by 0.260 nm, approximately 1/2 of the lattice parameter c of wurtzite-type ZnO [68]. This is equivalent to inserting one ZnO layer into a $(GaZn_m)O_{m+1}^+$ unit. Note that $InGaO_3(ZnO)_m$ and $Ga_2O_3(ZnO)_m$ exhibit different m-dependences, and consequently different rates of increase in their lattice parameter c, because their crystal systems differ: $InGa_2O_3(ZnO)_m$ and $Ga_2O_3(ZnO)_m$ are hexagonal and orthorhombic, respectively. For the orthorhombic

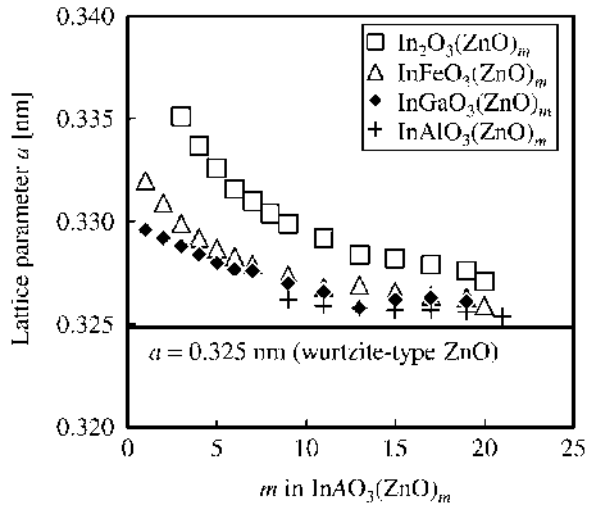

Figure 1.19 Lattice constant a as a function of m in hexagonal $InAO_3(ZnO)_m$ (A = In, Fe, Ga, and Al). Open squares, open triangles, filled rhombuses, and plus symbols denote series of homologous $In_2O_3(ZnO)_m$, $InFeO_3(ZnO)_m$, $InGaO_3(ZnO)_m$, and $InAlO_3(ZnO)_m$, respectively. *Source*: Adapted from [67]

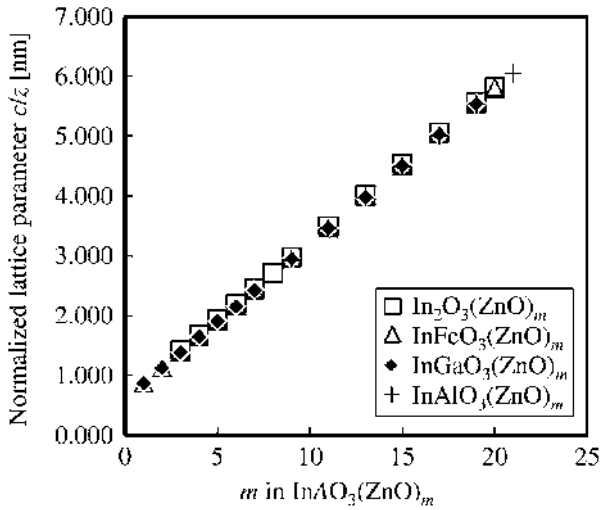

Figure 1.20 Lattice constant c as a function of m in hexagonal $InAO_3(ZnO)_m$ (A = In, Fe, Ga, and Al). The parameter z equals the number of formula units per unit cell. The normalized parameter c/z is the c-axis length per formula units. Open squares, open triangles, filled rhombuses, and plus symbols denote series of homologous $In_2O_3(ZnO)_m$, $InFeO_3(ZnO)_m$, $InGaO_3(ZnO)_m$, and $InAlO_3(ZnO)_m$, respectively. For each increment of m, the c-axis lengthens by approximately 0.263 nm. *Source*: Adapted from [67]

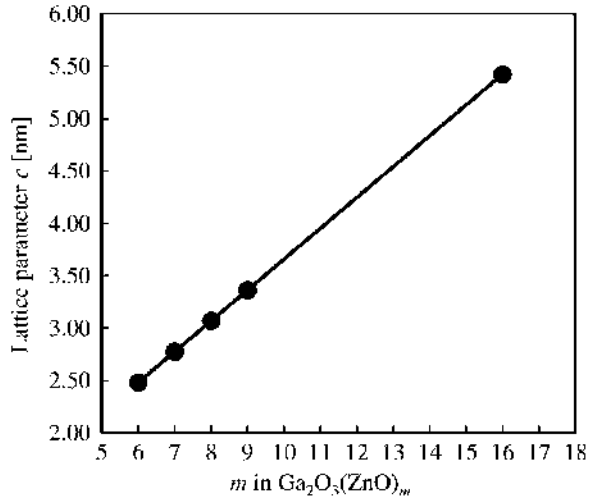

Figure 1.21 Relation between lattice constant c and m in $Ga_2O_3(ZnO)_m$ with an orthorhombic unit cell. The lattice constant c was determined from single-crystal data. For each increment of m, the c-axis lengthens by 0.294 nm. *Source*: Reprinted from [23], Copyright (1995), with permission from Elsevier

homologous forms $Ga_2O_3(ZnO)_m$, the c-axis lengthens at 0.294 nm per increment in m (Figure 1.21).

Solid solutions of $InAO_3(ZnO)_m$ exist between indium and element A. Figure 1.22 presents the composition dependence of the lattice parameters a and c and the volume V of solid solutions in $InGaO_3(ZnO)_m$ ($m = 1, 2, 3$, and 4). At high ratios of In^{3+} to $InGaO_3(ZnO)_m$ [i.e., when x in $In_{1+x}Ga_{1-x}O_3(ZnO)_m$ is large and positive], the lattice parameters a and c are large. Assuming that substituting In^{3+} for the Ga^{3+} lattice sites in $(GaZn_m)O^+_{m+1}$ units maintains the stoichiometric ratio, the varying lattice length can be attributed to the altered ionic radius.

In contrast, when the In^{3+} ratio in $InGaO_3(ZnO)_m$ is, in other words, when x in $In_{1+x}Ga_{1-x}O_3(ZnO)_m$ is large and negative, the lattice parameters a and c become small and large, respectively. Again, we assume that substituting Ga^{3+} for the In^{3+} lattice sites in InO_2^- units preserves the stoichiometric ratio. In this case, the O^{2-} octahedrons in the InO_2^- units should be small, and the lengths of the a- and c-axes will show different dependencies on In^{3+}. This suggests that lengthening the c-axis relaxes the stress caused by contraction along the (001) plane direction.

1.3.3 Structural Characteristics of $RAO_3(BO)_m$ Crystals

The crystal structure of compounds isostructural with homologous $RAO_3(BO)_m$ is characterized as follows [67].

i. All cations and anions reside on the triangular lattices. Cations fill three types of sites: octahedral sites (trivalent cations R), trigonal-bipyramid sites (trivalent cations A), and

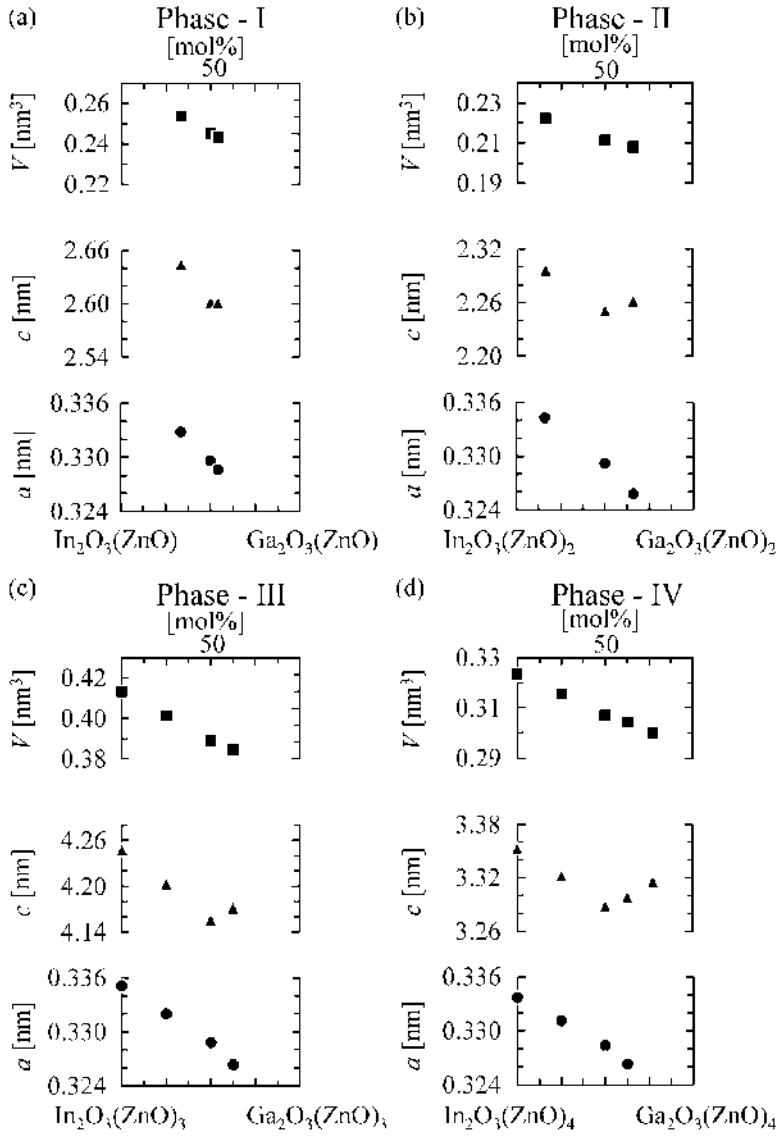

Figure 1.22 Hexagonal lattice constants *a* and *c* and unit cell volumes *V* of layered phases. (a) Phase I: $In_{1.33}Ga_{0.67}O_3(ZnO)$–$In_{0.92}Ga_{1.08}O_3(ZnO)$, (b) Phase II: $In_{1.68}Ga_{0.32}O_3(ZnO)_2$–$In_{0.68}Ga_{1.32}O_3(ZnO)_2$, (c) Phase III: $In_2O_3(ZnO)_3$–$In_{0.54}Ga_{1.46}O_3(ZnO)_3$, (d) Phase IV: $In_2O_3(ZnO)_4$–$In_{0.46}Ga_{1.54}O_3(ZnO)_4$. *Source*: Reprinted from [15], Copyright (1991), with permission from Elsevier

tetrahedral sites (divalent cations *B*). Compounds with a solid-solution range between the trivalent cations *R* and *A* have been found in $RAO_3(BO)_m$. The two-dimensional close-packing (and eutactic) O^{2-} layer is perpendicular to the *c*-axis in the hexagonal system.

ii. To explain the structure of homologous $RAO_3(BO)_m$, we consider a similar crystal. The octahedral site of $RAO_3(BO)_m$ is similar to the CdI_2-type structure. The trigonal-bipyramid or tetrahedral sites are analogous to, but not exactly the same as, wurtzite-type ZnO. Although the stacking sequence of cations and anions is inverted from the trigonal-bipyramid site, the tetrahedral site is similar to wurtzite-type ZnO. The ZnO layer is inserted perpendicular to the *c*-axis between the RO_2^- and AO^+ layers of $YAlO_3$-type RAO_3 (Figure 1.23). In particular, in homologous $RAO_3(BO)_m$ where *m* is even, the trigonal-bipyramid site is similar to the AO^+ layer of $YAlO_3$-type RAO_3.

iii. In homologous $InGaO_3(ZnO)_m$ (m = odd), which includes $InGaO_3(ZnO)$, the cations in the trigonal bipyramids reside slightly far from the common base of two pyramids; technically, between four- and five-coordination distant. In homologous $InGaO_3(ZnO)_m$ (m = even), the cations reside on the common base of two trigonal pyramids; technically, in the middle of the five-coordination.

$RAO_3(BO)$ is a member of homologous $RAO_3(BO)_m$. In addition, oxides with the general formula $RAO_3(BO)$ form K_2NiF_4-type, $CaFe_2O_4$-type, $YbFe_2O_4$-type, and spinel-type structures. When R = In, A = Ga, and B = Zn, they form a $YbFe_2O_4$-type structure; when R = In, A = Fe, and B = Co, they form a spinel-type structure. Thus, the constituent cations are limited by the characteristics of the $YbFe_2O_4$-type structure; that is, by the octahedrons and trigonal bipyramids with shared edges. In oxides, Ni^{2+} and Cr^{3+} have high selectivity for 6-fold coordination, and thus the compounds of such cations do not form layered-structure $RAO_3(BO)$. Furthermore, lanthanide elements that have a large ionic radius prevent edge-sharing of the trigonal bipyramids; consequently, these elements also prohibit layered-structure $RAO_3(BO)$.

1.4 Latest Topics in Crystalline IGZO

1.4.1 Interest in Non-conventional Compounds, $InGaO_3(ZnO)_m$ (m: non-integral number)

Section 1.3 described the crystal structures of In_2O_3–Ga_2O_3–ZnO systems with the compositional formula $InGaO_3(ZnO)_m$ (*m*: natural number), and their solid solutions. The composition ratio of a thin film deposited by conventional sputtering methods may differ from that of the sputtering target. In IGZO fabrication, the zinc composition fraction is smaller in the sputtered thin film than in the sputtering target. This means that if the sputtering target is $InGaO_3(ZnO)_m$ (*m*: natural number), the zinc composition fraction in the thin film is smaller than *m*, and may be non-integer.

How do the crystal structures of $InGaO_3(ZnO)_m$ (*m*: non-integer) differ from those of $InGaO_3(ZnO)_m$ (*m*: natural number)? This section presents the analytical results of various polycrystalline powders (Chapter 2 will describe the crystal structures of thin films deposited by sputtering methods). Here, polycrystalline IGZO with an In:Ga:Zn atomic ratio of 1:1:*x* is referred to as "IGZO(1:1:*x*)."

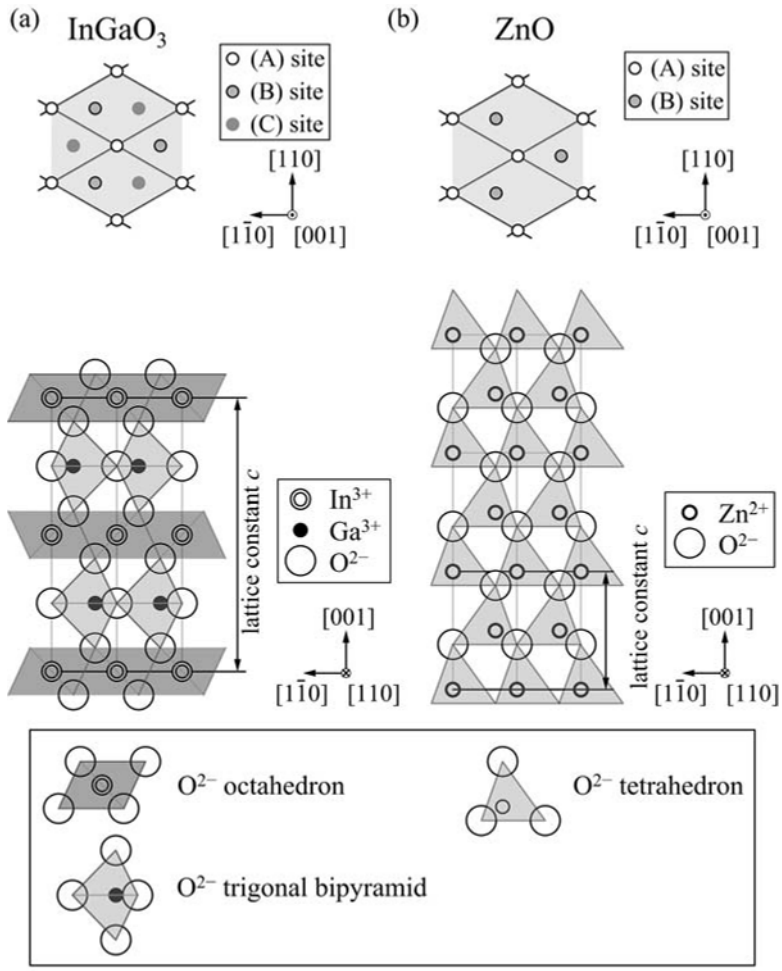

Figure 1.23 $YAlO_3$-type $InGaO_3$ [50] (a) and wurtzite-type ZnO [68] (b), projected onto the (001) and (110) planes. $InGaO_3$ isostructural with $YAlO_3$ forms under high pressure. *Source*: Adapted from [23]

1.4.2 Crystal Structures and Local Structures

The crystallinities of polycrystalline powder samples are conventionally determined by X-ray diffraction (XRD). Figure 1.24 shows the XRD spectrum of a sample synthesized by annealing mixed In_2O_3, Ga_2O_3, and ZnO raw powders at 1250°C in a dry air atmosphere. No peaks can be ascribed to In_2O_3, Ga_2O_3, or ZnO, indicating that all of the raw powders have reacted. All of the peaks in the XRD spectrum of the IGZO(1:1:1.5) polycrystalline powder can be assigned to the diffraction peaks of $InGaO_3(ZnO)$ or $InGaO_3(ZnO)_2$ (m = 1, 2). Therefore, IGZO(1:1:1.5) predominantly comprises $InGaO_3(ZnO)$ and $InGaO_3(ZnO)_2$ crystals. Phase separation frequently occurs in IGZO(1:1:1.5), as described in Section 1.3. No other phases are detected in the XRD

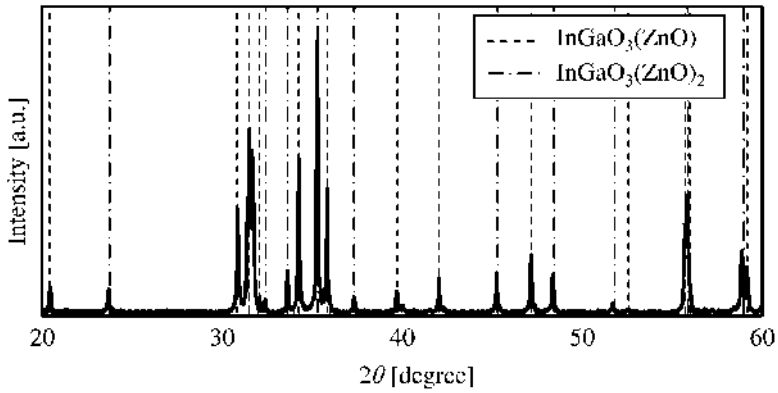

Figure 1.24 XRD spectrum of polycrystalline IGZO(1:1:1.5) powder

measurement, but XRD provides only average information over the area irradiated with an X-ray spot.

What structure appears in a microscopic view of IGZO(1:1:1.5)? Microscopic regions with areas smaller than 100 μm^2 and those with disordered structural defects yield no information in XRD analyses. To observe the local structure, it is required to use a powerful technique such as high-angle annular dark-field scanning transmission electron microscopy (HAADF-STEM). The details of this technique are described in Appendix 1.A.2.1. In a HAADF-STEM image, the luminance of a spot corresponding to a column of atoms is proportional to the square of its atomic number. Thus, the rows of indium atoms appear as rows of bright spots, because indium has the largest atomic number among the IGZO constituents. Gallium and zinc atoms appear as rows of relatively dim spots. Oxygen atoms are undetectable by HAADF-STEM, since their atomic number is smaller than the detection limit.

Figure 1.25 shows HAADF-STEM images obtained from three regions of a single-crystal grain. As described in Section 1.3, crystalline $InGaO_3(ZnO)_m$ has atomic layers consisting of indium and oxygen (hereafter called the InO_2^- layer) and $(m+1)$ layers consisting of gallium, zinc, and oxygen (hereafter called the (GaZn)O layer) sandwiched by two InO_2^- layers. In region (a) of Figure 1.25, there are only regions where three (GaZn)O layers are sandwiched by two InO_2 layers; that is, the crystalline structure in this region is that of $InGaO_3(ZnO)_2$ (hereafter called the triple (GaZn)O layer regions). Meanwhile, in regions (b) and (c) of the figure, there are some regions where two (GaZn)O layers are sandwiched by two InO_2^- layers (hereafter called the double (GaZn)O layer regions). The number of (GaZn)O layers varies spatially between two and three.

Such structures are observed not only in IGZO(1:1:1.5), but also in several IGZOs with various composition ratios. Figure 1.26 shows the XRD spectra and HAADF-STEM images of several IGZO$(1:1:m)$ $(1 \le m < 2)$ samples. The peaks in the XRD spectrum of each sample correspond to peaks of $InGaO_3(ZnO)$ or $InGaO_3(ZnO)_2$, apart from small shifts due to changes in the lattice constants. In these XRD spectra, the peaks at $2\theta = 34.3^\circ$ and $2\theta = 35.3^\circ$ are assigned to the (104) planes of the $InGaO_3(ZnO)$ crystal and the (014) plane of the $InGaO_3(ZnO)_2$ crystal, respectively. The fraction of zinc in the sample affects the intensity ratio between the two peaks; namely, the larger the zinc fraction, the higher the intensity of the peak

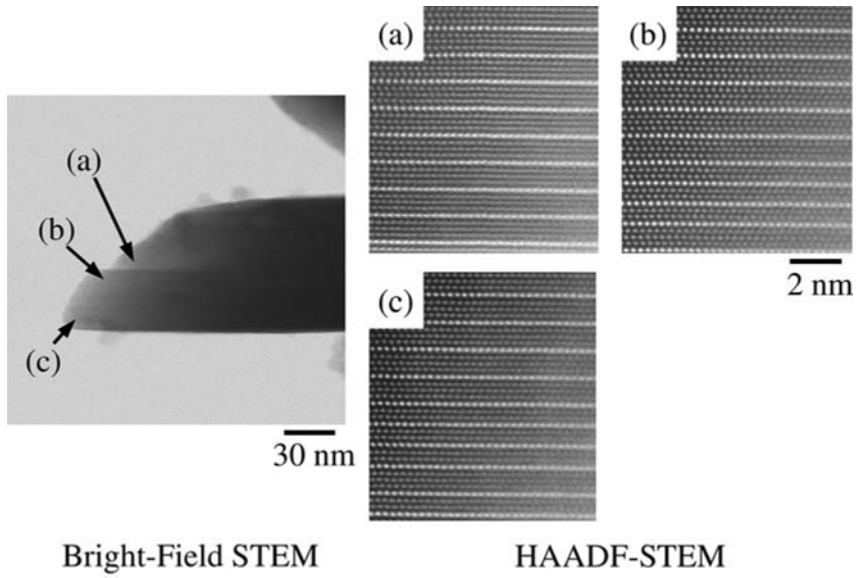

Figure 1.25 HAADF-STEM images of an IGZO(1:1:1.5) polycrystal. Each measurement point is part of a single-crystal grain

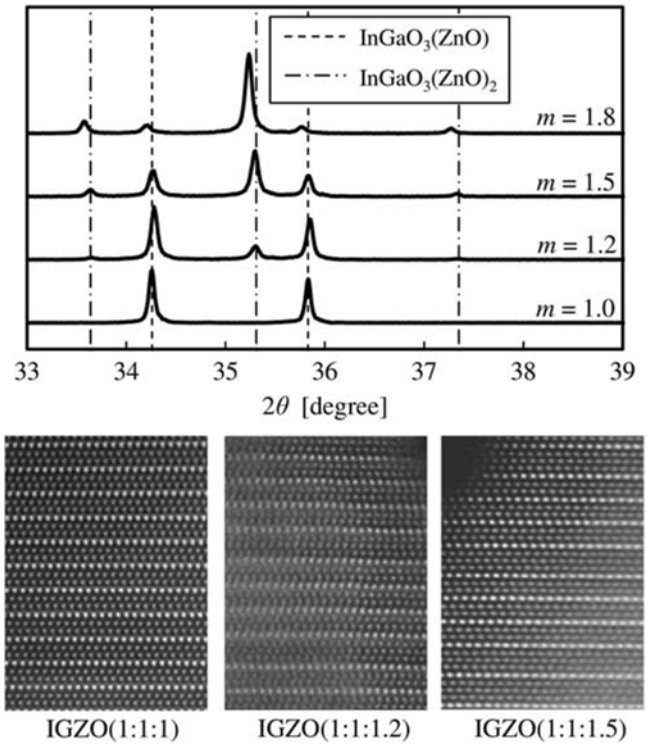

Figure 1.26 XRD spectra and HAADF-STEM images of $InGaO_3(ZnO)_m$ ($m = 1.0, 1.2, 1.5$). *(For color detail, please see color plate section)*

from the (014) plane of the $InGaO_3(ZnO)_2$ crystal. Thus, samples with high zinc content contain many $InGaO_3(ZnO)_2$ crystals.

The HAADF-STEM images of each sample reveal double (GaZn)O regions and triple (GaZn)O regions. In samples with larger zinc fractions, the triple (GaZn)O region becomes more common, consistent with the fraction of $InGaO_3(ZnO)_2$ patterns in XRD spectra.

1.4.3 Atomic Distribution in Crystalline IGZO(1:1:1.5)

Gallium and zinc atoms in $InGaO_3(ZnO)_m$ are known to be randomly arranged at five-coordinate sites in the (GaZn)O layers. Is this positional randomness maintained in the crystal structure of IGZO(1:1:1.5)? The configuration of gallium and zinc atoms which are randomly arranged in the five-coordinate positions of $InGaO_3(ZnO)_m$ crystals cannot be determined from XRD measurements. To determine their configurations in the IGZO (1:1:1.5) crystal, a scanning energy dispersive X-ray spectroscopy (EDX) measurement is employed.

Figure 1.27(a) and (b) presents an EDX line profile and a STEM image of an IGZO (1:1:1.5) crystal, respectively. Both analyses were conducted in the same measurement region. In the scanning EDX measurement, an electron beam is scanned along the *c*-axis direction (i.e., the direction perpendicular to the InO_2^- plane), and the cation composition at each point on the scanning line can be detected by the characteristic X-rays. The area selected for the scanning EDX includes both double and triple (GaZn)O regions. According to the EDX profile, the zinc fraction almost equals the gallium fraction in the double (GaZn)O region, but increases in the triple (GaZn)O region. The crystal structure of the double (GaZn)O region, in which the Ga/Zn ratio is nearly one, is similar to that of $InGaO_3(ZnO)$. Therefore, the crystal structure of IGZO(1:1:1.5) can be understood as a structure where pairs of zinc and oxygen atoms are inserted randomly into double (GaZn)O regions at the crystal base of $InGaO_3(ZnO)$, so that the whole composition fraction becomes In:Ga:Zn = 1:1:1.5 (atomic ratio) as shown in Figure 1.28. Note that the inserted atoms have a complicated arrangement, and zinc atoms are randomly placed in the triple (GaZn)O layers.

1.4.4 Influence of Composition of Crystalline IGZO

As described in Section 1.3, the compositional formula $InGaO_3(ZnO)_m$ (m: natural number) has been well studied as a homologous phase of the In_2O_3–Ga_2O_3–ZnO system. When m is non-integer, the crystal structure of $InGaO_3(ZnO)_m$ takes a specific form as described in Subsection 1.4.2, although in most regions of the crystal grains $InGaO_3(ZnO)_m$ (m: non-integer) is a composite of two or more $InGaO_3(ZnO)_m$ (m: natural number) crystal structures. Considering the solid-solution phase in Section 1.3, the most versatile compositional formula of the homologous phase of the In_2O_3–Ga_2O_3–ZnO system is $In_{1+x}Ga_{1-x}O_3(ZnO)_m$ ($-1 < x \leq 1$, m: non-integer). Note that the range of x is limited, depending on the zinc composition.

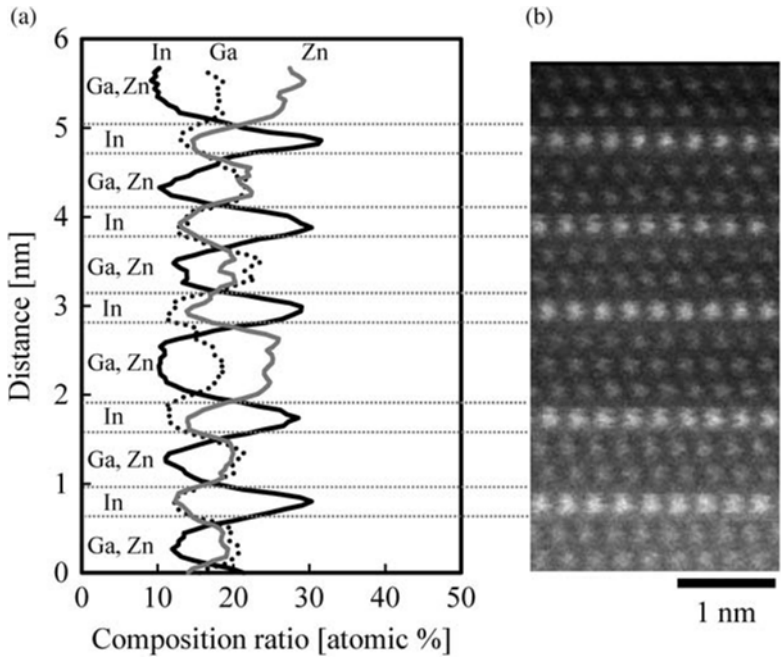

Figure 1.27 (a) EDX line profile and (b) HAADF-STEM image of IGZO(1:1:1.5) polycrystal

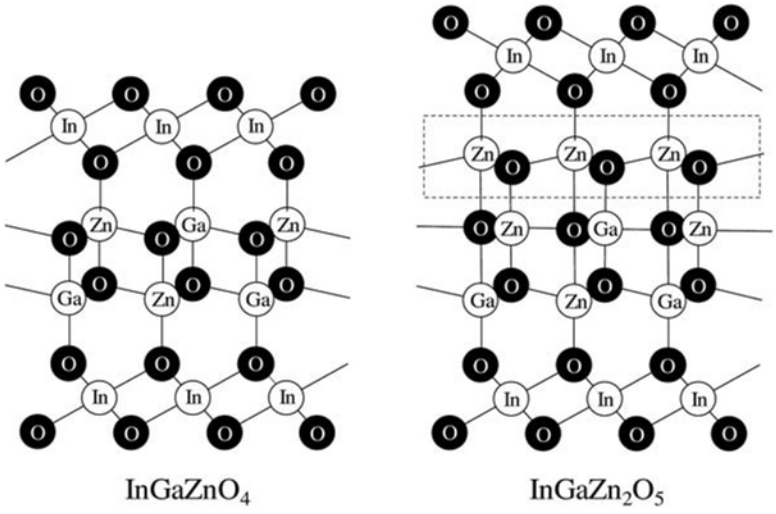

Figure 1.28 Schematics of crystal structures of double and triple (GaZn)O regions. In the triple (GaZn)O region, pairs of zinc and oxygen atoms are inserted between InO_2 layers into the double (GaZn)O structure. Note that the inserted layer (enclosed in the dotted rectangle) is comprised only of zinc cations and oxygen anions. In practice, this construct is much more complicated, and zinc atoms are randomly placed in the triple (GaZn)O layers

These types of crystal structures can be interpreted as an order–disorder metallic oxide phase [69], containing randomly inserted ZnO layers in the $InGaO_3(ZnO)$ structure. Although the inserted ZnO layers might be regarded as stacking faults, the layered structure remains close to that of $InGaO_3(ZnO)_m$ (m: natural number). In a layered structure, structural defects are less detrimental than a structure which contains a separate phase of polycrystalline ZnO.

As mentioned above, the crystal structure and physical properties of layered crystalline IGZO are insensitive to slight changes of composition. By virtue of this feature, crystalline IGZO thin films can be fabricated over a wide process margin, facilitating the development of mass-production techniques.

Appendix 1.A High-Angle Annular Dark-Field Scanning Transmission Electron Microscopy and Annular Bright-Field Scanning Transmission Electron Microscopy

The two major methods of transmission electron microscopy are: standard transmission electron microscopy (TEM) and scanning transmission electron microscopy (STEM) [70–72]. Figure 1.29 is a conceptual diagram showing the electromagnetic lens system difference between TEM and STEM. In this appendix, TEM and STEM are briefly explained first. Then, as STEM methods suitable for atomic-level observation, high-angle annular dark-field scanning transmission electron microscopy (HAADF-STEM) and annular bright-field scanning transmission electron microscopy (ABF-STEM) are introduced.

1.A.1 Transmission Electron Microscopy

In TEM analysis, a parallel electron beam is irradiated to a flake specimen. The electrons transmitted through the specimen form a magnified image. If the electrons are transmitted through

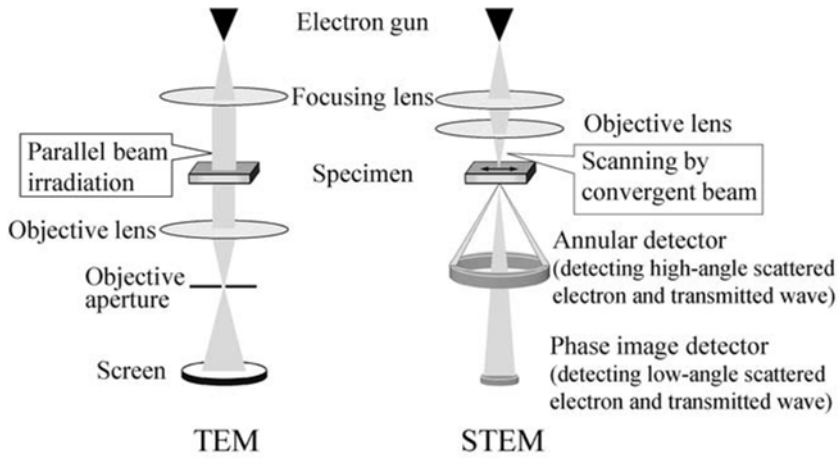

Figure 1.29 Conceptual diagram of electron optical system difference between TEM and STEM

the specimen without scattering or diffraction (transmitted waves), a bright-field image is obtained; conversely, if the electrons are diffracted in the specimen (diffracted waves), a dark-field image is obtained. A lattice image consists of lattice fringes formed by the interference between the transmitted diffracted waves. The lattice image reflects the crystal structure but does not correspond to the atom image.

1.A.2 Scanning Transmission Electron Microscopy

In STEM analysis, a flake specimen is two-dimensionally scanned by a convergent electron beam, and the intensity of the electrons transmitted through the specimen is measured by an annular detector. A STEM image is formed by synchronizing the two-dimensionally scanned positions and the detected intensities. If the transmitted and low-angle scattered electrons are detected, a bright-field STEM image (BF-STEM) is formed. A BF-STEM image contains approximately the same information as a bright-field TEM image. Conversely, if the transmitted electrons are detected and the high-angle scattered electrons are excluded, an annular dark-field STEM image (ADF-STEM) is obtained. In this mode, the high-angle scattered electrons are removed by the annular detector. The ADF-STEM image is less prone to electron wave interference than a bright-field image, and reflects the atomic number.

Among the various STEM methods, HAADF-STEM and ABF-STEM are suitable for atomic-level observation. Figure 1.30 is a conceptual diagram showing annular detector positions of HAADF-STEM and ABF-STEM. Figure 1.31 shows HAADF-STEM and ABF-STEM images of $InGaZnO_4$.

1.A.2.1 High-Angle Annular Dark-Field Scanning Transmission Electron Microscopy

Elastically scattered electrons transmitted through a flake specimen are distributed through higher angles than inelastically scattered electrons. The intensity as a function of scattering

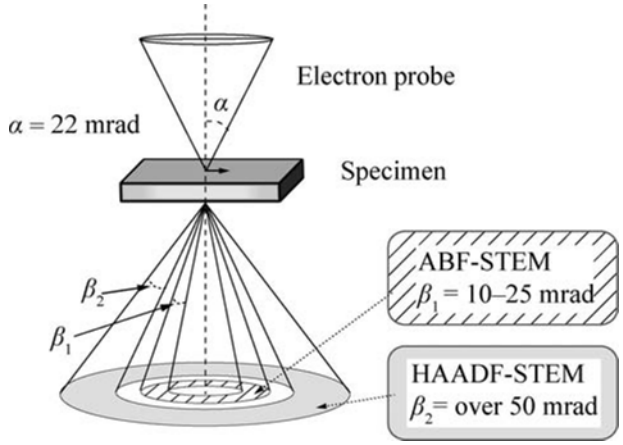

Figure 1.30 Conceptual diagram of annular detector position of HAADF-STEM and ABF-STEM

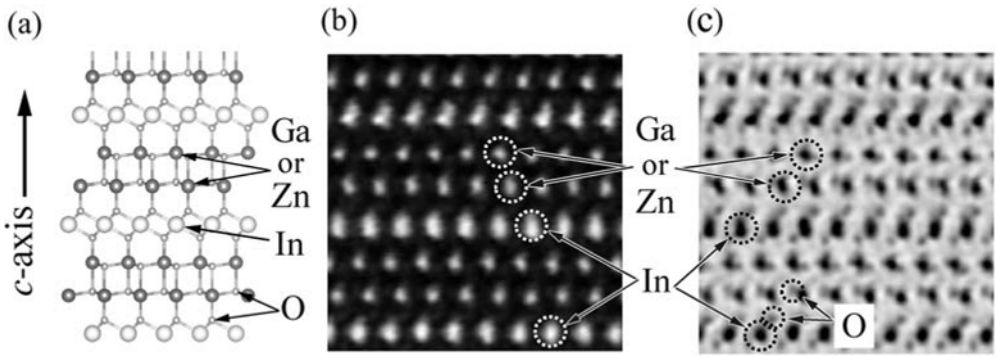

Figure 1.31 Observations by HAADF-STEM and ABF-STEM: (a) $InGaZnO_4$ crystal model, (b) a HAADF-STEM image, and (c) an ABF-STEM image

angle depends on the elements and density of the specimen. Atoms with large atomic number exhibit higher intensity at high angles than smaller atoms. HAADF-STEM exploits the different scattering intensities among elements in the high-angle region (generally 50 mrad or higher at 200 kV). HAADF-STEM images are incoherent, providing a direct interpretation. The image intensity is proportional to the product of the density ρ and the square of the atomic number; thus, we can quantify the image by analyzing its intensity. In addition, because HAADF-STEM images are free from diffraction effects, HAADF-STEM is suitable for observing materials without periodic structures.

1.A.2.2 Annular Bright-Field Scanning Transmission Electron Microscopy

In ABF-STEM imaging, a transmission beam with a collection semi-angle of 10 mrad or lower is cut by a beam stopper, and only the periphery of the transmission beam (generally 10 to 25 mrad at 200 kV) is detected. The focus depth and specimen thickness exert little effect on the image. ABF-STEM allows observation of light elements such as oxygen whereas HAADF-STEM can observe heavy elements clearly and can hardly detect the contrast of light elements. Unlike HAADF-STEM, the image contrast in ABF-STEM does not follow a simple scaling law corresponding to the atomic number. This is because the factors causing the image contrast in ABF-STEM are different between light elements and heavy elements. ABF-STEM is inferior to HAADF-STEM in intensity quantitativeness; however, ABF-STEM can effectively observe columns of light elements.

Atomic-level observations by HAADF-STEM and ABF-STEM have been improved by an aberration correction such as a spherical aberration correction lens.

In recent years, spherical aberration correction lenses (Cs corrector lenses) have been developed to improve the resolution of electron microscopy. A Cs lens relaxes the probe size limitation and preserves the electron beam current, which is otherwise reduced by spherical aberration of the electromagnetic lens. These improvements enable high-resolution observations and analyses down to the atomic level.

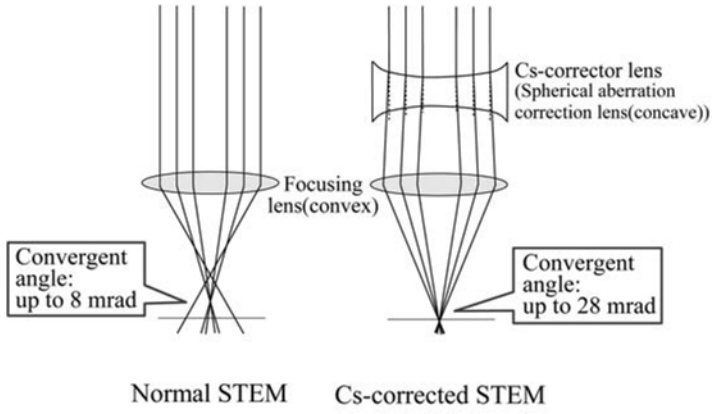

Figure 1.32 Comparison of conceptual diagrams between electronic optical system of normal STEM and that of Cs-corrected TEM

Figure 1.32 illustrates a comparison between normal STEM and Cs-corrected STEM. Spherical aberration, caused when the electrons in the electron beam follow different paths through the center and off-center parts of the lens, leads to indistinct images. This aberration increases the electron beam probe size decreases. Conventional electron microscopes always employ convex electromagnetic lenses (see the left-hand figure in Figure 1.32). However, a concave electromagnetic lens formed by multipoles is now available to be used with the convex electromagnetic lenses, which corrects for spherical aberration (see the right-hand figure in Figure 1.32). This correction technique further boosts the spatial resolution of TEM/STEM analysis.

References

[1] Weiher, R. L. and Lev, R. P. (1966) "Optical properties of indium oxide," *J. Appl. Phys.*, **37**, 299.
[2] Walsh, A., Da Silva, J. L. F., Wei, S.-H., Körvber, C., Klein, A., Piper, L. F. J., *et al*. (2008) "Nature of the band gap of In_2O_3 revealed by first-principles calculations and X-ray spectroscopy," *Phys. Rev. Lett.*, **100**, 167402.
[3] Mang, A., Reinmann, K., and Rübenacke, St. (1995) "Band gaps, crystal-field splitting, spin-orbit coupling, and exciton binding energies in ZnO under hydrostatic pressure," *Solid State Commun.*, **94**, 251.
[4] Tippins, H. H. (1965) "Optical absorption and photoconductivity in the band edge of β-Ga_2O_3," *Phys. Rev.*, **140**, A316.
[5] Roth, R. S. (1957) "Classification of perovskite and other ABO_3-type compounds," *J. Res. Natl. Bur. Stand.*, **58**, 75.
[6] Roth, R. S. and Schneider, S. J. (1960) "Phase equilibria in systems involving the rare-earth oxides. Part I. Polymorphism of the oxides of trivalent rare-earth ions," *J. Res. Natl. Bur. Stand.*, **64A**, 309.
[7] Schneider, S. J., Roth, R. S., and Waring, J. L. (1961) "Solid state reactions involving oxides of trivalent cations," *J. Res. Natl. Bur. Stand.*, **65A**, 345.
[8] Kimizuka, N. and Mohri, T. (1985) "Spinel, $YbFe_2O_4$, and $Yb_2Fe_3O_7$ types of structures for compounds in the In_2O_3 and Sc_2O_3–A_2O_3–BO systems [*A*: Fe, Ga, or Al; *B*: Mg, Mn, Fe, Ni, Cu, or Zn] at temperatures over 1000°C," *J. Solid State Chem.*, **60**, 382.
[9] Kimizuka, N. and Takayama, E. (1988) "The phase relations in the In_2O_3–A_2O_3–BO systems at elevated temperatures [*A*: Fe or Ga, *B*: Cu or Co]," *J. Solid State Chem.*, **53**, 217.

[10] Kimizuka, N., Mohri, T., and Matsui, Y. (1988) "Homologous compounds, $InFeO_3(ZnO)_m$ (m = 1–9)," *J. Solid State Chem.*, **74**, 98.
[11] Kimizuka, N. and Mohri, T. (1989) "Structural classification of $RAO_3(MO)_n$ compounds [R = Sc, In, Y or lanthanides; A = Fe(III), Ga, Cr or Al; M = divalent cation; n = 1–11]," *J. Solid State Chem.*, **78**, 98.
[12] Kimizuka, N., Mohri, T., and Nakamura, M. (1989) "Compounds which have $InFeO_3(ZnO)_m$-type of structures (m = integer)," *J. Solid State Chem.*, **81**, 70.
[13] Kimizuka, N., Mohri, T., and Nakamura, M. (1990) "The phase relations in the system In_2O_3–A_2BO_4–BO at elevated temperatures (A: Fe, Ga, Cr; B: Mg, Co, Ni or Cu): Part II," *J. Solid State Chem.*, **87**, 449.
[14] Nakamura, M., Kimizuka, N., and Mohri, T. (1990) "The phase relations in the In_2O_3–Fe_2ZnO_4–ZnO system at 1350°C," *J. Solid State Chem.*, **86**, 16.
[15] Nakamura, M., Kimizuka, N., and Mohri, T. (1991) "The phase relations in the In_2O_3–Ga_2ZnO_4–ZnO system at 1350°C," *J. Solid State Chem.*, **93**, 298.
[16] Nakamura, M., Kimizuka, N., Mohri, T., and Isobe, M. (1993) "The phase relations in the In_2O_3–Al_2ZnO_4–ZnO system at 1350°C," *J. Solid State Chem.*, **105**, 535.
[17] Kimizuka, N., Takayama-Muromachi, E., and Siratori, K. (1990) "Chapter 90, The systems R_2O_3–M_2O_3–M′O," in Gschneidner Jr., K. A. and Eyring, L. (Eds.), *Handbook on the Physics and Chemistry of Rare Earths*, Vol. **13**. Amsterdam: North-Holland, pp. 283–384.
[18] Kato, K., Kawada, I., Kimizuka, N., and Katsura, T. (1975) "Die Kristallstruktur von $YbFe_2O_4$," *Z. Kristallogr.*, **141**, 314.
[19] Shindo, I., Kimizuka, N., and Kimura, S. (1976) "Growth of YFe_2O_4 single crystals by floating zone method," *Mater. Res. Bull.*, **11**, 637.
[20] Iida, J. (1990) "Single crystal growth of $LuFe_2O_4$, $LuFeCoO_4$, and $YbFeMgO_4$ by the floating zone method," *J. Cryst. Growth*, **102**, 398.
[21] Kimizuka, N., Nakamura, M., and Mohri, T. (1993) "Syntheses and crystallographic data of homologous compounds, $InFeO_3(ZnO)_m$ (m = 1, 2, 3, 7, 11, 13, 15, and 19) and $Fe_2O_3(ZnO)_m$ (m = 8 and 9) in the In_2O_3–Fe_2ZnO_4–ZnO system," *J. Solid State Chem.*, **103**, 394.
[22] Isobe, M., Kimizuka, N., Nakamura, M., and Mohri, T. (1994) "Structures of $LuFeO_3(ZnO)_m$ (m = 1, 4, 5 and 6)," *Acta Crystallogr. Sec. C*, **50**, 332.
[23] Kimizuka, N., Isobe, M., and Nakayama, M. (1995) "Syntheses and single-crystal data of homologous compounds, $In_2O_3(ZnO)_m$ (m = 3, 4 and 5), $InGaO_3(ZnO)_3$, and $Ga_2O_3(ZnO)_m$ (m = 7, 8, 9 and 16) in the In_2O_3–$ZnGa_2O_4$–ZnO system," *J. Solid State Chem.*, **116**, 170.
[24] Wells, A. F. (1975) *Structural Inorganic Chemistry*, 4th edn. Oxford: Clarendon Press.
[25] Jeffrey, G. A. and Wu, V. Y. (1963) "The structure of the aluminum carbonitrides," *Acta Cryst.*, **16**, 559.
[26] Jeffrey, G. A. and Wu, V. Y. (1966) "The structure of the aluminum carbonitrides. II," *Acta Cryst.*, **20**, 538.
[27] Haeuseler, H. and Srivastava, S. K. (2000) "Phase equilibria and layered phases in the systems A_2X_3–M_2X_3–M′X (A = Ga, In; M = trivalent metal; M′ = divalent metal; X = S, Se)," *Z. Kristallogr.*, **215**, 205.
[28] Kimizuka, N. and Katsura, T. (1975) "Standard free energy of formation of $YFeO_3$, $Y_3Fe_5O_{12}$, and a new compound YFe_2O_4 in the Fe–Fe_2O_3–Y_2O_3 system at 1200°C," *J. Solid State Chem.*, **13**, 176.
[29] Kimizuka, N. and Katsura, T. (1975) "The standard free energy of formation of $YbFe_2O_4$, $Yb_2Fe_3O_7$, $YbFeO_3$, and $Yb_3Fe_5O_{12}$ at 1200°C," *J. Solid State Chem.*, **15**, 151.
[30] Kitayama, K. and Katsura, T. (1976) "Phase equilibria in Fe–Fe_2O_3–Ln_2O_3 (Ln = Sm and Er) systems at 1200°C," *Bull. Chem. Soc. Jpn.*, **49**, 998.
[31] Sekine, T. and Katsura, T. (1976) "Phase equilibria in the system Fe–Fe_2O_3–Lu_2O_3 at 1200°C," *J. Solid State Chem.*, **17**, 49.
[32] Katsura, T., Sekine, T., Kitayama, K., and Sugihara, T. (1978) "Thermodynamic properties of Fe–lathanoid–O compounds at high temperatures," *J. Solid State Chem.*, **23**, 43.
[33] Kasper, H. (1967) "Neuartige Phasen mit würtzitärhnlichen Strukturen im System ZnO–In_2O_3," *Z. Anorg. Allg. Chem.*, **349**, 113.
[34] Cannard, P. J. and Tilley, J. D. (1988) "New intergrowth phases in the ZnO–In_2O_3 system," *J. Solid State Chem.*, **73**, 418.
[35] Dupont, L., Maugy, C., Naghavi, N., Guery, C., and Tarascon, J.-M. (2001) "Structures and textures of transparent conducting pulsed laser deposited In_2O_3–ZnO thin films revealed by transmission electron microscopy," *J. Solid State Chem.*, **158**, 119.
[36] McCoy, M. A., Grimes, R. W., and Lee, W. E. (1997) "Planar intergrowth structures in the ZnO–In_2O_3 system," *Philos. Mag. A*, **76**, 1187.

[37] Moriga, T., Edwards, D. D., Mason, T. O., Palmer, G. B., Poeppelmeier, K. R., Schindler, J. L., *et al*. (1998) "Phase relationships and physical properties of homologous compounds in the zinc oxide–indium oxide system," *J. Am. Ceram. Soc.*, **81**, 1310.
[38] Gerardin, R., Alebouyeh, A., Brice, J. F., Evrard, O., and Sanchez, J. P. (1988) "Distribution cationique dans les ferrites d'indium de type spinelle In*M*FeO_4 (*M* = Ni, Mn, Co, Mg)," *J. Solid State Chem.*, **76**, 398.
[39] Moriga, T., Kammler, D. R., Mason, T. O., Palmer, G. B., and Poeppelmeier, K. R. (1999) "Electrical and optical properties of transparent conducting homologous compounds in the indium–gallium–zinc oxides system," *J. Am. Ceram. Soc.*, **82**, 2705.
[40] Shannon, R. D. (1976) "Revised effective ionic radii and systematic studies of interatomic distances in halides and chalcogenides," *Acta Crystallogr. Sec. A*, **32**, 751.
[41] Matsui, Y. (1980) "Extra electron reflections observed in YFe_2O_4, $YbFe_2O_4$, $Yb_2Fe_3O_7$ and $Yb_3Fe_4O_{10}$," *J. Appl. Crystallogr.*, **13**, 395.
[42] Kato, K., Kawada, I., Kimizuka, N., Shindo, I., and Katsura, T. (1976) "Die Kristallstruktur von $Yb_2Fe_3O_7$," *Z. Kristallogr.*, **143**, 278.
[43] Kimizuka, N., Kato, K., Shindo, I., Kawada, I., and Katsura, T. (1976) "New compounds of $Yb_3Fe_4O_{10}$ and $Yb_4Fe_5O_{13}$," *Acta Crystallogr. Sec. B*, **32**, 1620.
[44] Matsui, Y., Kato, K., Kimizuka, N., and Horiuchi, S. (1979) "Structure image of $Yb_3Fe_4O_{10}$ by a 1 MV high-resolution electron microscope," *Acta Crystallogr. Sec. B*, **35**, 561.
[45] Hill, R. J., Craig, J. R., and Gibbs, G. V. (1979) "Systematics of the spinel structure type," *Phys. Chem. Miner.*, **4**, 317.
[46] Michiue, Y., Kimizuka, N., and Kanke, Y. (2008) "Structure of $Ga_2O_3(ZnO)_6$: A member of the homologous series $Ga_2O_3(ZnO)_m$," *Acta Crystallogr. Sec. B*, **64**, 521.
[47] Michiue, Y. and Kimizuka, N. (2010) "Superspace description of the homologous series $Ga_2O_3(ZnO)_m$," *Acta Crystallogr. Sec. B*, **66**, 117.
[48] Michiue, Y., Kimizuka, N., Kanke, Y., and Mori, T. (2012) "Structure of $(Ga_2O_3)_2(ZnO)_{13}$ and a unified description of the homologous series $(Ga_2O_3)_2(ZnO)_{2n+1}$," *Acta Crystallogr. Sec. B*, **68**, 250.
[49] Li, C., Bando, Y., Nakamura, M., Kurashima, K., and Kimizuka, N. (1999) "Structure analysis of new homologous compounds $Ga_2O_3(ZnO)_m$ (m = integer) by high-resolution analytical transmission electron microscopy," *Acta Crystallogr. Sec. B*, **55**, 355.
[50] Shannon, R. D. and Prewitt, C. T. (1968) "Synthesis and structure of phases in the In_2O_3–Ga_2O_3 system," *J. Inorg. Nucl. Chem.*, **30**, 1389.
[51] Barbier, J. (1989) "$In_{1.2}Ga_{0.8}MgO_4$: Powder neutron refinement and crystal chemistry," *J. Solid State Chem.*, **82**, 115.
[52] Moriga, T., Sakamoto, T., Sato, Y., Haris, A. H. K., Suenari, R., and Nakabayashi, I. (1999) "Crystal structures and electrical and optical properties of $MgIn_{2-x}Ga_xO_4$ solid solutions," *J. Solid State Chem.*, **142**, 206.
[53] Freund, H.-R. and Müller-Buschbaum, Hk. (1978) "Üer Oxocuprate. XXV Zur Kenntnis von $In_2Cu_2O_5$," *Z. Anorg. Allg. Chem.*, **441**, 103.
[54] Nakamura, M. and Kimizuka, N. (1993) "$In(Ti_{1/2}M_{1/2}O_3(MO)_m$ compounds (M = Zn or Mg, *m*. natural number): Synthesis and crystal structures," *Jpn. J. Appl. Phys. Suppl.*, **32**, 184.
[55] Eichhom, S. and Mader, W. (2016) "Structure and optical properties of $[In_{1-2x}Sn_xZn_x]GaO_3(ZnO)_m$," *J. Solid State Chem.*, **233**, 75.
[56] Malaman, B., Evrard, O., Tannières, N., and Coutrois, A. (1975) "Structure crystalline de la phase $Yb_{0.5}Eu_{0.5}Fe_2O_4$," *Acta Crystallogr. Sec. B*, **31**, 1310.
[57] Gerardin, R., Alebouyeh, A., Jeannot, F., Courtois, A., Malaman, B., and Evrard, O. (1980) "Sur l'existence des oxydes rhomboe driques A(III)B(II)B′(III)O_4," *Mater. Res. Bull.*, **15**, 647.
[58] Isobe, M., Kimizuka, N., Iida, J., and Takekawa, S. (1990) "Structure of $LuFeCoO_4$ and $LuFe_2O_4$," *Acta Crystallogr. Sec. C*, **46**, 1917.
[59] Nespolo, M., Isobe, M., Iida, J., and Kimizuka, N. (2000) "Crystal structure and charge distribution of $ErFeMnO_4$," *J. Alloy. Comp.*, **313**, 59.
[60] Nespolo, M., Sato, A., Osawa, T., and Ohashi, H. (2000) "Synthesis, crystal structure and charge distribution of $InGaZnO_4$, X-ray diffraction study of 20 kb single crystal and 50 kb twin by reticular merohedry," *Cryst. Res. Technol.*, **35**, 151.
[61] Assenmacher, W., Schnakenburg, G., Michiue, Y., Kanke, Y., Kimizuka, N., and Mader, W. (2014) "Synthesis and crystal structure characterization of $InGaZnO_4$ with a new defect structure," *J. Solid State Chem.*, **215**, 176.
[62] O'Keeffe, M. (1977) "On the arrangements of ions in crystals," *Acta Crystallogr. Sec. A*, **33**, 924.

[63] Keller, I., Assenmacher, W., Schnakenburg, G., and Mader, W. (2009) "Synthesis and crystal structures of $InGaO_3(ZnO)_m$ ($m = 2$ and 3)," *Z. Anorg. Allg. Chem.*, **635**, 2065.
[64] Keller, I. and Mader, W. (2010) "The crystal structure of $InGaO_3(ZnO)_4$: A single crystal X-ray and electron diffraction study," *Z. Anorg. Allg. Chem.*, **636**, 1045.
[65] Lee, W.-J., Choi, E.-A., Bang, J., Ryu, B., and Chang, K. J. (2008) "Structural and electronic properties of crystalline $InGaO_3(ZnO)_m$," *Appl. Phys. Lett.*, **93**, 111901.
[66] Da Silva, J. L. F., Yan, Y., and Wei, S.-H. (2008) "Rules of structure formation for the homologous $InMO_3(ZnO)_n$ compounds," *Phys. Rev. Lett.*, **100**, 255501.
[67] Nakamura, M., Kimizuka, N., Mohri, T., and Isobe, M. (1993) "Syntheses and crystal structures of new homologous compounds, indium iron zinc oxides ($InFeO_3(ZnO)_m$) (m: natural number) and related compounds," *KOTAI BUTSURI (Solid State Physics)*, **28**, 317 [in Japanese].
[68] Abrahams, S. C. and Bernstein, J. L. (1969) "Remeasurement of the structure of hexagonal ZnO," *Acta Crystallogr. Sec. B*, **25**, 1233.
[69] Yokobayashi, H., Kishida, K., Inui, H., Yamasaki, M., and Kawamura, Y. (2011) "Enrichment of Gd and Al atoms in the quadruple close packed planes and their in-plane long-range ordering in the long period stacking-ordered phase in the Mg–Al–Gd system," *Acta Mater.*, **59**, 7287.
[70] Findlay, S. D., Shibata, N., Sawada, H., Okunishi, E., Kondo, Y., Yamamoto, T., *et al*. (2009) "Robust atomic resolution imaging of light elements using scanning transmission electron microscopy," *Appl. Phys. Lett.*, **95**, 191913.
[71] Findlay, S. D., Shibata, N., Sawada, H., Okunishi, E., Kondo, Y., and Ikuhara, Y. (2010) "Dynamics of annular bright field imaging in scanning transmission electron microscopy," *Ultramicroscopy*, **110**, 903.
[72] Williams, D. B. and Carter, C. B. (2009) *Transmission Electron Microscopy: A Textbook for Materials Science*, 2nd edn. New York: Springer.